Journal of
Nanoscience and Nanotechnology
Vol. 8,27-55, 2007

Oxide Nanobelts and Nanowires—Growth, Properties and Applications

Zhong Lin Wang

School of Materials Science and Engineering, Georgia Institute of Technology, Atlanta, GA 30332-0245, USA

Nanowires (NWs) and nanobelts (NBs) are diverse classes of one-dimensional nanoscale materials with controllable size, composition, structure and corresponding physical and chemical properties. This article reviews the novel growth phenomena, unique properties and exciting applications of oxide NWs and NBs. First, the article gives a general introduction about the vapor-liquid-solid (VLS) growth method. Second, the growth of oxide NBs using a vapor-solid (VS) process has been demonstrated. Third, using ZnO as an example, polar-surface dominated growth phenomena, such as the formation of single-crystal nanoring, nanospring and nanohelix, are comprehensively described. Then, novel techniques developed for characterizing the mechanical, electrical, thermal and optical properties of NWs and NBs are illustrated. Finally, some exciting applications in areas such as sensors, photon detectors and nanogenerators are presented. In concluding, the challenges and prospects for the future are discussed.

Keywords:

RESEARCH ARTICLE

1. INTRODUCTION

One-dimensional (1D) nanostructures have ~~also~~ been the focus of extensive studies worldwide in the last decade due to their unique physical properties and potential to revolutionize broad areas of nanotechnology.[1] There are three main types of 1D nanomaterials: carbon nanotubes,[2–12] semiconductor nanowires,[13–20] and semiconducting oxide nanobelts.[21–23]

Semiconducting nanowires (NWs)[13,14] represent an important and broad class of nanometer scale wire structure, which can be rationally and predictably synthesized in single crystal form with all key parameters controlled during growth: chemical composition, diameter, length, and doping.[15–17] Semiconductor NWs thus represent one of best-defined and controlled classes of nanoscale building blocks, which correspondingly have enabled a wide-range of devices and integration strategies to be pursued in a rational manner. For example, semiconductor NWs have been assembled into nanometer scale field effect transistors (FETs),[17,18,24,25] p-n diodes,[18,19] light emitting diodes (LEDs),[18] bipolar junction transistors,[19] complementary inverters,[19] complex logic gates and even computational circuits that have been used to carry out basic digital calculations.[20] In contrast to NTs, NW devices can be assembled in a rational and predictable manner because the size, interfacial properties, and electronic properties of the NWs can be precisely controlled during synthesis, and moreover, reliable methods exist for their parallel assembly.[26] In addition, it should be recognized that it is possible to combine distinct NW building blocks in ways not possible in conventional electronics and to leverage the knowledge base that exists for the chemical modification of inorganic surfaces[27,28] to produce semiconductor NW devices that achieve new function and correspondingly could lead to unexpected device concepts.

Semiconducting oxide nanobelts (NBs) are another unique group of quasi-one-dimensional nanomaterials, which have been systematically studied for a wide range of materials with distinct chemical composition and crystallographic structures. Belt-like, quasi-one-dimensional nanostructures (so called nanobelts or nanoribbons) have been synthesized for semiconducting oxides of zinc, tin, indium, cadmium and gallium, by simply evaporating the desired commercial metal oxide powders at high temperatures.[21] The as-synthesized oxide nanobelts are pure, structurally uniform, single crystalline and most of them free from dislocations; they have a rectangular-like cross-section with constable dimension. The belt-like morphology appears to be a unique and common structural characteristic for the family of semiconducting oxides with cations of different valence states and materials of distinct crystallographic structures. Field effect transistors[29] and ultra-sensitive nano-size gas sensors,[30] nanoresonators[31] and nanocantilevers[32] have also been

 1533-4880/2007/8/027/055 doi:10.1166/jnn.2007.N08

fabricated based on individual nanobelts. Thermal transport along the nanobelt has also been measured.[33] Very recently, nanobelts, nanosprings[23,34] and nanorings[35] that exhibit piezoelectric properties have been synthesized, which could be a candidate for nano-scale traducers, actuators and sensors.

With consideration the diversity of the field[36] this review will mainly focus on the synthesis, structure analysis, novel properties and selected applications of oxide NWs and NBs. First, we will discuss rational design of synthetic strategies and the synthesis of NWs via a vapor-liquid-solid (VLS) growth mechanism. Secondly, the vapor-solid process for synthesis of oxide based nanostructures will be described in details. We will illustrate the polar surface dominated growth phenomena, such as the formation of nanosprings, nanorings and nanohelices of single-crystal zinc oxide. Third, we will describe the unique and novel electrical, optoelectronic, field emission, mechanical and thermal properties of individual NWs and NBs. Finally, we will illustrate some novel devices and applications made using NWs as ultra-sensitive chemical and biological nanosensors, cross-wire junction based devices, nanogenerators, and nano-piezotronics.

2. SYNTHESIS OF OXIDE NANOWIRES AND NANOBELTS

2.1. VLS Approach to Nanowires Using Catalyst Particles

A general strategy that has received increasing focus over that past several years involves exploiting a 'catalyst' to confine growth in 1D. Depending on the phases involved in the reaction, this approach is typically defined as vapor-liquid-solid (VLS),[37,38] solution-liquid-solid (SLS),[39,40] or vapor-solid (VS)[41,42] growth.

VLS is one of the most popular and powerful growth of NWs (Fig. 1), in which the catalyst particle is used to direct 1D growth of single crystal materials.[13,14] Here the catalyst is envisioned as a nanocluster or nanodroplet that defines in most of cases the diameter of and serves as the site that directs preferentially the addition of reactant to the end of a growing NW much like a living polymerization catalyst directs the addition of monomers to a growing

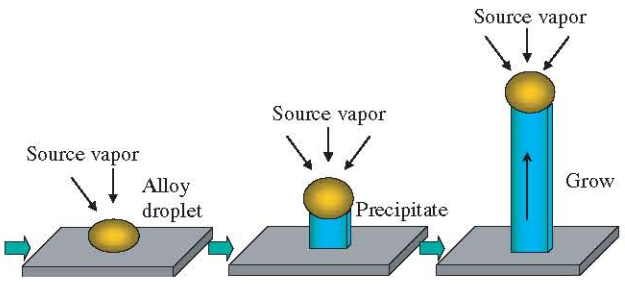

Fig. 1. Schematic diagram showing the growth of aligned nanowire arrays via the vapor-liquid-solid process.

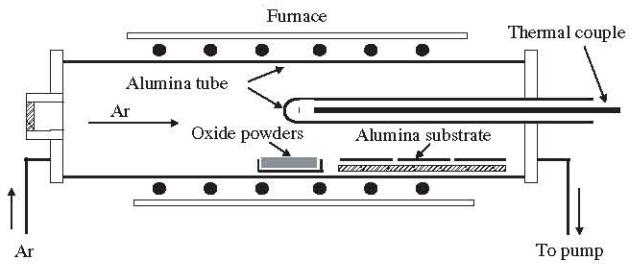

Fig. 2. Schematic diagram of experimental apparatus for growth of oxides nanostructures.

polymer chain. In principle, the vapor-solid technique is a simple process in which condensed or powder source material(s) is vaporized at elevating temperature and then the resultant vapor phase(s) condenses at certain conditions (temperature, pressure, atmosphere, substrate, etc.) to form the desired product(s). The processes are usually conducted in a tube furnace, as shown in Figure 2. It consists of a horizontal tube furnace, a rotary pump system and a gas supply and control system. A view window is set up at the left end of the alumina tube, which is used to monitor the growth process. The right end of the alumina tube is connected to the rotary pump. Both ends are sealed by rubber O-rings. The ultimate vacuum for this configuration is $\sim 2 \times 10^{-3}$ Torr. The carrying gas comes in from the left end of the alumina tube and is pumped out at the right end. The source material(s) is loaded on an alumina boat and positioned at the center of the alumina tube. Several alumina strip plates (60×10 mm) were placed downstream one-by-one inside the alumina tube, which acted as substrates for collecting growth products.

There are several processing parameters such as temperature, pressure, carrier gas (including gas species and its flow rate), substrate and evaporation time period, which can be controlled and need to be selected properly before and/or during the thermal evaporation. The source temperature selection mainly depends on volatility of the source material(s). The pressure is determined according to evaporation rate or vapor pressure of source material(s). The substrate temperature usually drops as the distance of its location away from the position of source material(s). The far the distance is, the lower the substrate temperature is. Of course, the temperature field in the furnace tube can be changed and controlled by introducing cold finger/plate or by using a multiple-zone furnace. Selecting a proper evaporation time is also important because it influences on not only the amount but also the size and the morphology of the product(s). It is also noted that the thermal evaporation process is very sensitive to the concentration of oxygen in the growth system.[43] Oxygen influences on not only the volatility of the source material(s), the stoichiometry of the vapor phase, but also formation of product(s). In the present study, after evacuating the alumina tube to $\sim 2 \times 10^{-3}$ Torr, thermal evaporation was conducted at a certain temperature for 2 hours under the conditions of

RESEARCH ARTICLE

a pressure of 200–600 Torr and an Ar carrier gas of 50 sccm (standard cubic centimeters per minute).

Growth of 1D nanostructure usually follows the vapor-liquid-solid (VLS) approach, in which a liquid alloy droplet composed of a metal catalyst component (such as Au, Fe) and a nanowire component (such as Si, III–V compound, II–V compound, oxide) is first formed under the reaction conditions. The metal catalyst can be rationally chosen from the phase diagram by identifying metals in which the nanowire component elements are soluble in the liquid phase but do not form solid compounds more stable than the desired nanowire phase. For the 1D ZnO nanowires grown via a VLS process, the commonly used catalyst for ZnO is Au.[44] As a result, a nanowire obtained from the VLS process typically has a solid catalyst nanoparticle at its tip with a diameter comparable to that of the connected nanowires.

Growth of patterned and aligned 1D nanostructures is important for applications in sensing,[45, 46] optoelectronics[47] and field emission.[48, 49] Aligned growth of ZnO nanorods has been successfully achieved on a solid substrate via a vapor-liquid-solid (VLS) process with the use of gold[50, 51] and tin[52] as catalysts, in which the catalyst initiates and guides the growth, and the epitaxial orientation relationship between the nanorods and the substrate leads to the aligned growth. Other techniques that do not use any catalyst, such as metalorganic vapor-phase epitaxial growth,[53] template-assisted growth and electrical field alignment[54] have also been employed for the growth of vertical aligned ZnO nanorods. Using nanowire as template, epitaxial growth on its surface can fabrication nanotubes of complex oxides[55, 56] Kempa et al. have demonstrated a technique of growing periodically arranged carbon nanotubes using a catalyst pattern produced from a mask with the use of self-assembled sub-micron spheres.[57, 58] Here we have combined the self-assembly based mask technique with the surface epitaxial approach to grow large-area hexagonal arrays of aligned ZnO nanorods.[59]

The synthesis process involves three main steps. The hexagonally patterned ZnO nanorod arrays are grown on a single crystal Al_2O_3 substrate, on which patterned Au catalyst particles are dispersed. First, a two-dimensional, large-area, self-assembled and ordered monolayer of sub-micron spheres was formed on a single crystal Al_2O_3 substrate (Fig. 3(a)). Second, a thin layer of gold particles was deposited onto the self-assembled monolayer (Fig. 3(b)); and then the spheres were etched away, leaving a patterned gold catalyst array (Fig. 3(c)). Finally, NWs were grown

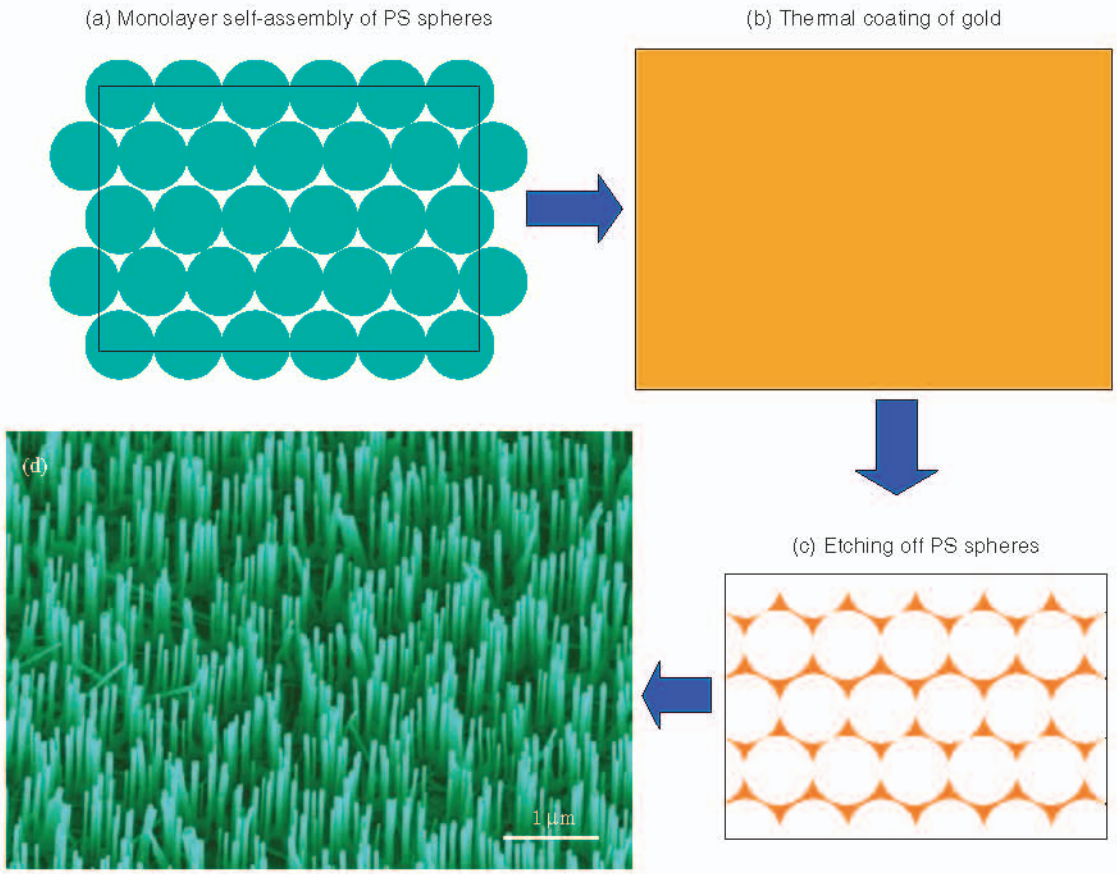

Fig. 3. Schematic experimental procedure for growth of aligned nanowires. (a) Self-assembled monolayer of polystyrene spheres forming a mask. (b) Deposition of gold catalyst by thermal evaporation. (c) Removal of polystyrene spheres forming a hexagonal patterned catalyst. (d) Aligned ZnO nanowire grown on a single crystal alumina substrate with honeycomb pattern defined by the catalyst mask.

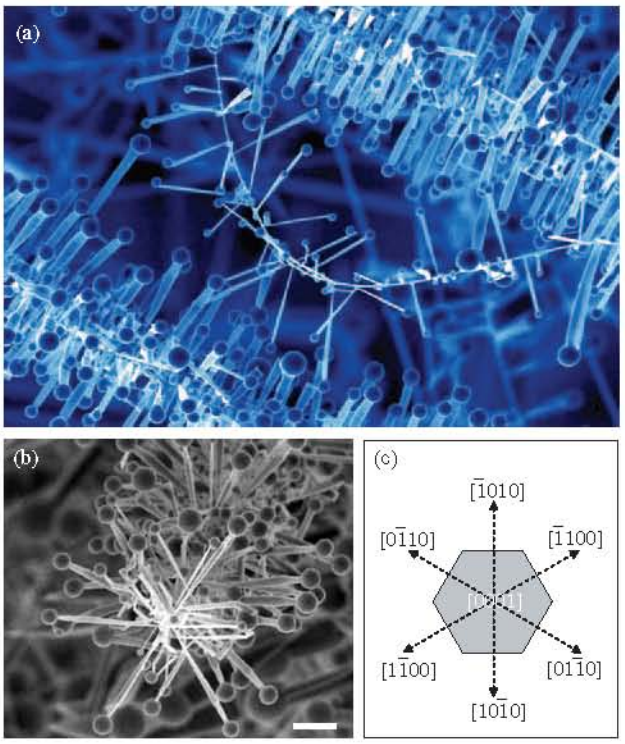

Fig. 4. (a) Multi-branched ZnO nanostructures grown by VLS using Sn as catalyst. (b) The front view of the nanostructure, showing quasi six-fold of symmetry. (c) Schematic diagram presenting an explanation about the formation of the nanostructure.

on the substrate using the VLS process (Fig. 3(d)). The spatial distribution of the catalyst particles determines the pattern of the nanowires to be grown. This step can be achieved using a variety of mast technology for producing complex configurations. By choosing the optimum match between the substrate lattice and the NW to be grown, the epitaxial orientation relationship between the nanowire and the substrate results in the aligned growth of nanowires normal to the substrate. The [0001] nanowires of ZnO presented in Figure 3(d) were grown on the $(2\bar{1}\bar{1}0)$ surface of single-crystal sapphire substrate. The distribution of the catalyst particles defines the location of the NWs, and the epitaxial growth on the substrate results in the vertical alignment.

Metal particle catalyzed growth of NWs can form various configurations depending the location and density of the catalyst. Figure 4(a) shows a low-magnification image of the as-synthesized ZnO nanowire structure using Sn as catalyst.[60] The morphology of the string appears like a "liana," and the axial nanowire is the "rattan," which has a uniform cross-section with dimension in the range of a few tens of nanometer. The "tadpole-like" branches have spherical balls at the tips. An interesting phenomenon observed in Figure 4(b) is that the distribution of the nanoribbons around the axial nanowire has an angle interval of $\sim 60°$. A typical front view of the nanowire indicates a six-fold symmetrical ordered assembly. The ZnO nanowire is likely to have a hexagonal cross-section bounded by $\pm(10\bar{1}0)$, $\pm(01\bar{1}0)$ and $\pm(\bar{1}100)$, which are six crystallographic equivalent planes. The Sn liquid droplets deposited onto the ZnO nanowire lead to the simultaneous growth of the ZnO nanoribbons along the six growth directions: $\pm[10\bar{1}0]$, $\pm[0\bar{1}10]$ and $\pm[\bar{1}100]$ (Fig. 4(c)). The angles between the two adjacent growth directions is 60°, resulting in the six-fold symmetric distribution of the nanoribbons around the nanowire.

2.2. Nanowires Grown from Large Gallium Surface

Growth of aligned nanowires is critical to practical applications. A general approach uses the nanoparticle guided growth through the VLS process, in which one particle nucleates one nanowire and the size of the particle determines the diameter of the nanowire. But we have shown that a large size (5 to 50 μm in diameter), low melting point gallium droplet can be used as an effective catalyst for the large-scale growth of highly aligned, closely packed silica nanowire bunches (Figs. 5(a, b)).[61] The growth was carried out using GaN powders, which were placed at the center of an alumina tube. A long silicon wafer stripe was placed in the middle part of a wide alumina plate. After evacuating the alumina tube to $\sim 2 \times 10^{-3}$ Torr, the reaction is conducted at 1150 °C for 5 hours under a pressure of 400 Torr and Ar gas flow rate of 50 sccm (standard cubic centimeters per minutes). At the reaction temperature of 1150 °C, the GaN powders are decomposed into a dense, hot vapor of Ga and N_2. The hot Ga vapor rapidly condenses into small Ga clusters as the Ga species cool through collision with the buffer gas. The formed Ga clusters are transferred to the downstream end of the alumina tube by the carrier gas, and then deposited onto the surface of the silicon wafer and the naked part of the alumina plate in the regions with temperatures <1070 °C. Our results show that Ga droplets with diameters <1 μm can be evenly distributed on the surfaces of the silicon wafer and alumina plate at the early reaction stage; however, the diameters of the Ga droplets increase with the reaction time through continuously accepting the upcoming Ga clusters, and are typically in the range of 5 to 50 μm after 5 hours reaction. The Ga droplets deposited on the silicon wafer etch silicon to form Ga-Si alloy and thus create a dense vapor of Si species around the silicon wafer and alumina plate, which acts as Si source for the growth of SiO_2 nanowires.

The silica nanowires tend to grow batch by batch. For each batch, numerous nanowires simultaneously nucleate, grow at nearly the same rate and direction, and simultaneously stop growing. Tubes whose wall is composed of highly aligned silica nanowires with diameters of 15 to 30 nanometers and length of 10 to 40 micrometers were obtained (Fig. 5(b)). One of the most amazing phenomenon observed is the self-splitting of the silica nanowire, as shown in Figure 5(c), which has not been observed in

RESEARCH ARTICLE

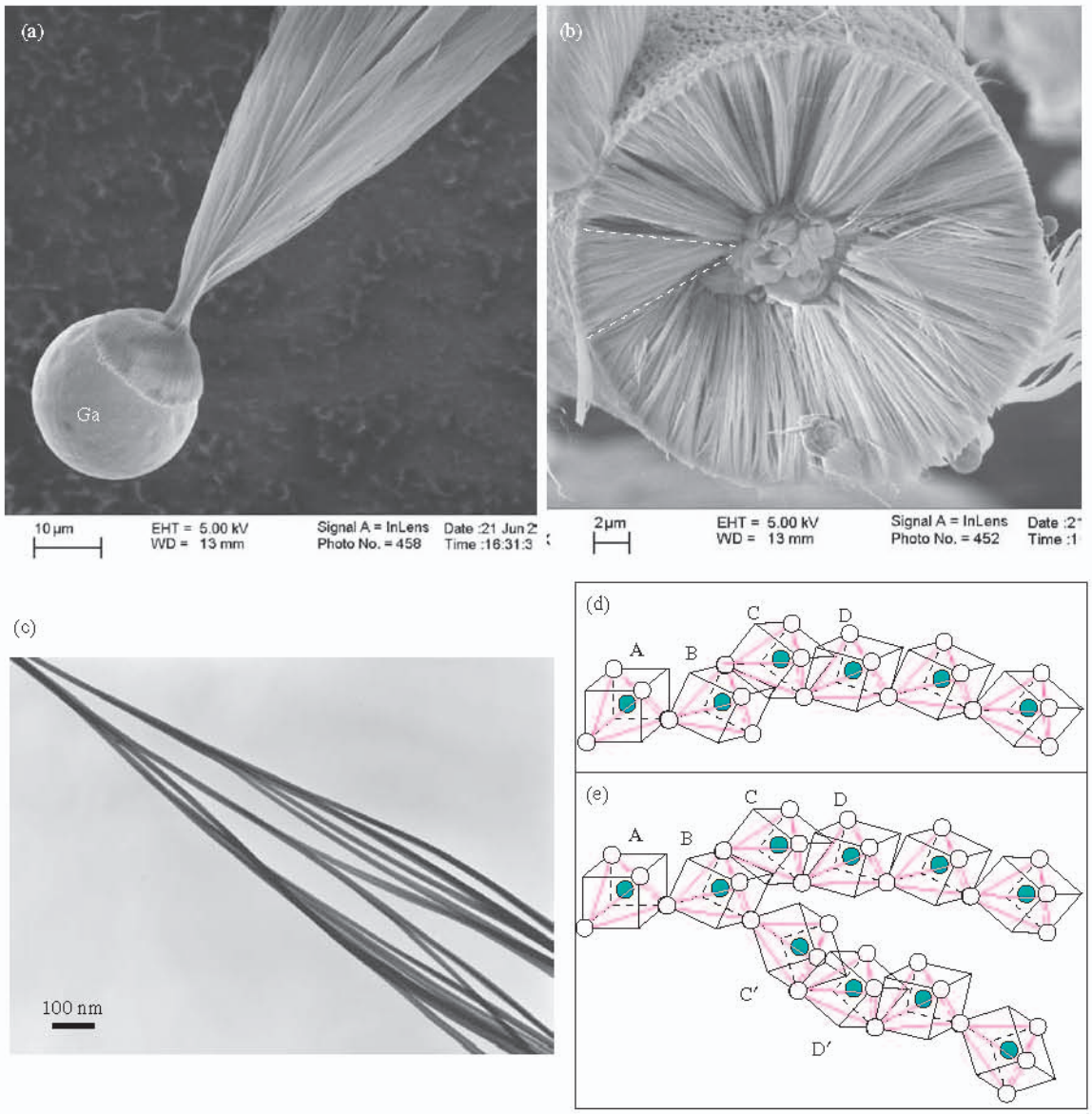

Fig. 5. (a, b) Aligned silica nanowires synthesized by evaporating GaN with the presence of a silicon substrate. The Ga droplet serves as the catalyst that leads to the nucleation and growth of uniform silica nanowires of diameters ~100 nm. (c) The silica nanowires have the characteristic of self-splitting, resulting in thicker bundles as the growth proceeds. (d) Interpretation about the self-splitting process of the silica glass structure.

crystalline nanowires. To offer a simple interpretation about the formation of wire splitting, we first examine the five Zachariasens' rules for oxide glass formation:[62]

(1) Oxide glass networks are composed of oxygen polyhedra;
(2) The coordination number of each oxygen atom is 2;
(3) The coordination number of each metal atom is 3 or 4;
(4) Oxygen polyhedra share corners, not edges or faces; and
(5) Each polyhedron must share at least three corners.

The polyhedron for silica is $(SiO_4)^{4-}$, which is a tetrahedron. The glass is formed by sharing corners of the tetrahedral, but without translation or orientation symmetry (Fig. 5(d)). We take tetrahedron B as an example, which has four corners to share. If this tetrahedron is on the surface of the nanowire, another tetrahedron C′ can be linked to B via corner sharing, a continuous growth along C′ and D′ leads to the formation of another nanowire.[63] The splitting of the nanowire may offers a new approach at nanoscale for splitting or converging optical signals using the silica nanowires. This is likely to be the reason that the density of the silica nanowires can be adjusted according to the geometry and available space to create a wide range of nanostructures, such as the diatoms found in nature.

2.3. Vapor-Solid Process Synthesis of Nanobelts

Vapor-solid growth process is a simple and effective method for the growth of oxide nanostructures without

using catalyst. There are two approach for vaporizing the source material, thermal vaporization and laser ablation. The thermal vaporization technique is a simple process, in which powder source material(s) is vaporized at elevating temperature and then the resultant vapor phase(s) condenses under certain conditions (temperature, pressure, atmosphere, substrate, etc.) to form the desired product(s). The morphology and phase structure of the synthesized product(s) depend on the source materials, growth temperature, temperature gradient, substrate, gas flow rate and pressure. Through our experiments, we found that the most sensitive and important parameters for controlling the purity of the growth product are growth temperature, kinetics and source materials.

Controlling experimental conditions are the key for controlling the synthesized product. The selection of the source temperature mainly depends on volatility of the source material(s). It is usually set to be ~300 °C lower than the bulk melting point of the source material. The pressure is determined according to evaporation rate or vapor pressure of source material(s). The substrate temperature usually drops as the distance of its location away from the position of source material(s). The far the distance is, the lower the substrate temperature is. Of course, the temperature field in the furnace tube can be changed and controlled by introducing cold finger/plate or by using a multiple-zone furnace. Selecting a proper evaporation time is also important because it influences not only the amount but also the size and the morphology of the product(s). It is also noted that the thermal evaporation process is very sensitive to the concentration of oxygen in the growth system. Oxygen influences not only the volatility of the source material(s), the stoichiometry of the vapor phase, but also type of product(s) to be synthesized.

In the family of nanobelts nanoribbons (see Table I), ZnO is probably the most extensively studied structures. Thermal evaporation of ZnO powders (purity: 99.99%; melting point: 1975 °C) at 1400 °C resulted in ultralong ZnO nanobelts (Fig. 6(a)). The as-synthesized oxide nanobelts are pure, structurally uniform, single crystalline

Table I. Some common oxide nanobelts and their growth directions and surface planes.

Nanobelts	Crystal structure	Growth direction/plane	Top surfaces	Side surfaces
ZnO	Wurtzite	[0001]	$\pm(2\bar{1}\bar{1}0)$	$\pm(01\bar{1}0)$
ZnO	Wurtzite	$[01\bar{1}0]$	$\pm(2\bar{1}\bar{1}0)$	$\pm(0001)$
ZnO	Wurtzite	[0001]	$\pm(2\bar{1}\bar{1}0)$	$\pm(01\bar{1}0)$
Ga_2O_3	Monoclinic	(010)	$\pm(100)$	$\pm(10\bar{1})$
Ga_2O_3	Monoclinic	(001)	$\pm(100)$	$\pm(010)$
SnO_2	Rutile	[101]	$\pm(10\bar{1})$	$\pm(010)$
In_2O_3	C-Rare earth	[001]	$\pm(100)$	$\pm(010)$
CdO	NaCl	[001]	$\pm(100)$	$\pm(010)$
PbO_2	Rutile	[010]	(201)	$\pm(10\bar{1})$
ZnS	Wurtzite	$[01\bar{1}0]$	$\pm(2\bar{1}\bar{1}0)$	$\pm(0001)$
CdSe	Wurtzite	$[01\bar{1}0]$	$\pm(2\bar{1}\bar{1}0)$	$\pm(0001)$

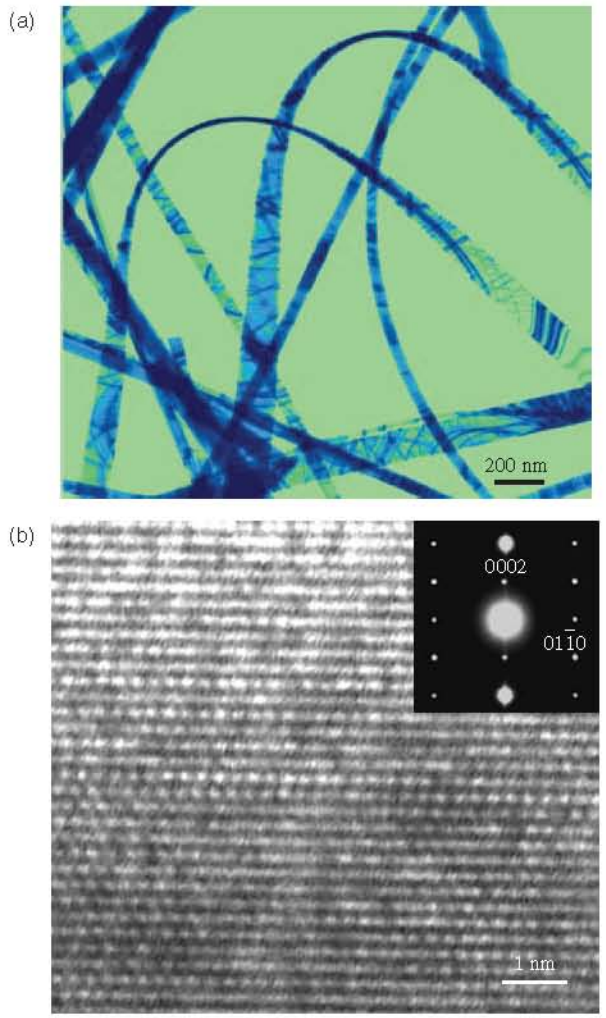

Fig. 6. TEM image of the as-synthesized ZnO nanobelts and a high-resolution TEM image recorded with the incident electron perpendicular to the top surface of the nanobelt.

and most of them free from dislocations. A ripple-like contrast appeared in the TEM image is due to strain resulted from the bending of the belt. Occasionally, some planar defects, such as twins and stacking faults are found, but there is no line defect.[64] Point defects, such as oxygen vacancies, should be present, which greatly affect the transport properties of the NBs. The NBs have a rectangular-like cross-section with typical widths of 30–300 nm, width-to-thickness ratios of 5–10 and lengths of up to a few millimeters. EDS and XRD measurements show that the sample is Wurtzite (hexagonal) structured ZnO with lattice constant of $a = 3.249$ Å and $c = 5.206$ Å, consistent with the standard values for bulk ZnO. No particle was observed at the ends of the nanobelts. High-resolution TEM (HRTEM) and electron diffraction studies show that the ZnO nanobelts are structurally uniform and single crystalline (Fig. 6(b)).

The belt-like morphology appears to be a unique and common structural characteristic for the family of

RESEARCH ARTICLE

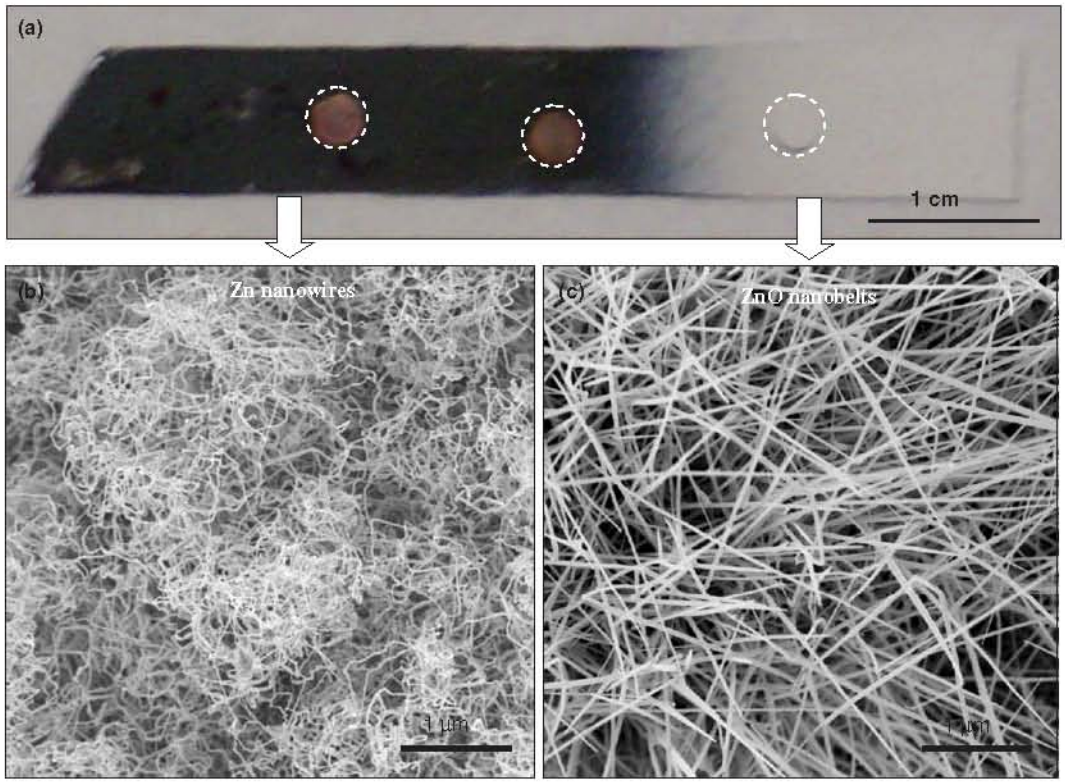

Fig. 7. (a) An optical micrograph of the as-synthesized sample on a silicon substrate, showing two distinct products on the surface. The three circles indicate three TEM copper grids placed on the substrate for collecting samples. (b, c) SEM images recorded from the metallic luster and white color regions, presenting the formation of pure Zn nanobelts and ZnO nanobelts, ~~respectively. (d) XRD recorded from the metallic region, showing the formation of Zn nanobelts~~.

semiconducting oxides with cations of different valence states and materials of distinct crystallographic structures. Nanobelts were successfully synthesized for a series of oxides with different valence states and different crystal structures, including ZnO,[21] SnO_2,[21] In_2O_3,[21] CdO,[21] Ga_2O_3,[65] and PbO_2.[66] The nanobelts were synthesized by vaporizing the corresponding oxide powder ~~a~~ without using catalyst. The surface morphologies of these nanostructures can be apparently identified from the SEM images.

2.4. Growth Kinetics

It is known that growth kinetics plays a key role in determining the morphology of nanostructures, but a limited knowledge is available for understanding the complex kinetics in VS growth. Controlling local temperature is probably the most important parameter for controlling the grown nanostructure. Figure 7(a) shows an optical image of the nanostructures deposited on a substrate by vaporizing ZnO powders.[67] The most interesting phenomenon is that the as-grown products are distributed at two distinct temperature regions, with the metallic luster in black color being the Zn nanobelts and the white color being the ZnO nanobelts. The two products were formed in the same growth chamber but they are clearly separated. Scanning electron microscopy (SEM) images show curly Zn nanobelts (Fig. 7(b)) and straight ZnO nanobelts (Fig. 7(c)). The Zn nanobelts were formed in a temperature range of 200–300 °C, and they are distributed across a region of >4 cm in length. The ZnO nanobelts were formed in a temperature range of 300–400 °C. The transition distance between the two different products is ~0.5 cm. This apparently shows the structural control by growth temperature and kinetics.

As for the result presented in Figure 7, our synthesis experiment used ZnO powder as the raw material, while the produced products were Zn nanowires and ZnO nanowires distributed in distinct temperature regions. It is well known that the decomposition of ZnO occurs when it is subject to high enough temperature in vacuum. The thermodynamics of these processes can be presented as the follows. The solid-vapor process and the decomposition process are expressed to be:

$$\mathrm{ZnO\,(s)} \leftrightarrow \mathrm{ZnO\,(g)} \tag{1}$$

$$\mathrm{ZnO\,(g)} \leftrightarrow \mathrm{Zn\,(g)} + \frac{1}{2}\mathrm{O_2\,(g)} \tag{2}$$

The equilibrium constant function K_p for processes (1) and (2) as a function of temperature is given by[68]

$$-R\ln K_p(T) = \Delta H^0_{298}/T + \Delta G(T) \tag{3}$$

where ΔH is the change in free energy and $\Delta G(T)$ the Gibbs energy, and $K_p = (P_{Zn(g)} \cdot P_{O_2}^{1/2})/P_e^{3/2}$, where P_{Zn} and P_{O_2} are the partial pressures of Zn and O_2, respectively, and P_e is the pressure in the growth chamber. Substituting the thermodynamic data into (3), one receives

$$\ln(P_{Zn(g)} \cdot P_{O_2}^{1/2}/P_e^{3/2}) = -4.855 - 2474/T \qquad (4)$$

From Eq. (4), the saturation vapor pressure for Zn at 1350 °C is estimated to be $\sim 10^{-3}$ torr, close to the pre-evacuated pressure in the growth chamber, hence, it is possible that part of the ZnO vapor decomposes into Zn vapor and O_2. Then, the ZnO vapor together with the Zn vapor are transported by Ar carrier gas to a lower temperature region of 200–400 °C, which is cold enough to condense the vapor phase onto the substrate. The ZnO vapor condenses in the region of 300–400 °C due to its higher sublimation temperature, resulting in the growth of ZnO nanobelts (the white region in Fig. 7(a)); the Zn vapor condenses in the 200–300 °C region owing to lower sublimation temperature, resulting in the growth of Zn nanobelts.

3. POLAR SURFACE INDUCED NOVEL GROWTH PHENOMENA

Although the entire unit cell of a crystal is neutrial, the distribution of the cations and anions could take specific configuration as determined by crystallography. For some oxides, such as MgO, NiO and ZnO, the cations and anions in oxides can produce surfaces that have net positive/negative charges. The polar charge dominated surfaces can give some unique growth phenomena. We now use ZnO to illustrate the unique characteristics of polar surfaces. Zinc oxide has a hexagonal structure (space group *C6mc*) with lattice parameters $a = 0.3296$, and $c = 0.52065$ nm. The structure of ZnO can be simply described as a number of alternating planes composed of tetrahedrally coordinated O^{2-} and Zn^{2+} ions, stacked alternatively along the *c*-axis (Fig. 8(a)). The tetrahedral coordination in ZnO results in non-central symmetric structure and piezoelectricity. Another important characteristic of ZnO is the polar surfaces. The most common polar surface is the basal plane. The oppositely charged ions produce positively charged Zn-(0001) and negatively charged O-(000$\bar{1}$) polar surfaces, resulting in a normal dipole moment and spontaneous polarization along the *c*-axis as well as a divergence in surface energy. To maintain a stable structure, the polar surfaces generally have facets or exhibit massive surface reconstructions, but ZnO ±(0001) are exception, which are atomically flat, stable and without reconstruction.[69, 70] Understanding the superior stability of the ZnO ±(0001) polar surfaces is a forefront research in today's surface physics.[71–74]

Another polar surface is the {01$\bar{1}$1}. By projecting the structure along [1$\bar{2}$10], as shown in Figure 16(b), beside the most typical ±(0001) polar surfaces that are

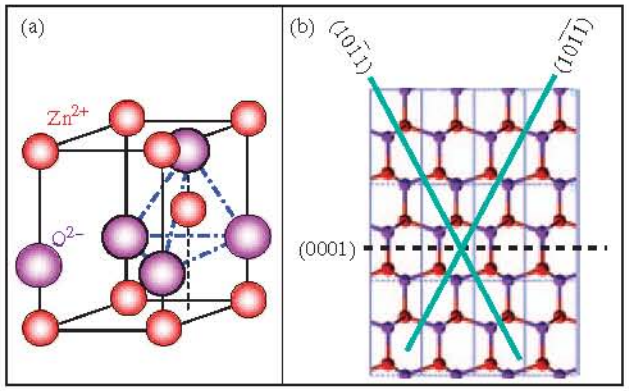

Fig. 8. (a) Wurtzite structure model of ZnO, which has non-central symmetry and piezoelectric effect. (b) The three types of facets of ZnO nanostructures: ±(0001), {2$\bar{1}\bar{1}$0} and {01$\bar{1}$0}.

terminated with Zn and oxygen, respectively, ±(10$\bar{1}$1) and ±(10$\bar{1}\bar{1}$) are also polar surfaces. The {10$\bar{1}\bar{1}$} type surfaces are not common for ZnO, but they have been observed in a nanohelical structure found recently.[75] The charges on the polar surfaces are ionic charges, which are non-transferable and non-flowable. Because the interaction energy among the charges depends on the distribution of the charges, the structure is arranged in such a configuration to minimize the electrostatic energy. This is the main driving force for growing the polar surface dominated nanostructures.

3.1. Nanospiral and Nanosprings

Due to differences in surface energies among (0001), {01$\bar{1}$0} and {2$\bar{1}\bar{1}$0}, freestanding nanobelts and nanowires of ZnO are usually dominated by the lower energy, non-polar surfaces such as {01$\bar{1}$0} and {2$\bar{1}\bar{1}$0}. Recently, by introducing doping, such as In and/or Li, ZnO nanobelts dominated by the (0001) polar surfaces have been grown. The nanobelt grows along [2$\bar{1}\bar{1}$0] (the *a*-axis), with its top/bottom large surface ±(0001) and the side surfaces ±(01$\bar{1}$0). Due to the small thickness of 5–20 nm and large aspect ratio of ~1:4, the flexibility and toughness of the nanobelts are extremely high. A polar surface dominated nanobelt can be approximated to be a capacitor with two parallel charged plates (Fig. 9(a)). The polar nanobelt tends to roll over into an enclosed ring to reduce the electrostatic energy (Fig. 9(b)). A spiral shape is also possible for reducing the electrostatic energy (Fig. 9(c)).[76] The formation of the nanorings and nanohelixes can be understood from the nature of the polar surfaces. If the surface charges are uncompensated during the growth, the spontaneous polarization induces electrostatic energy due to the dipole moment, but rolling up to form a circular ring would minimize or neutralize the overall dipole moment, reducing the electrostatic energy. On the other hand, bending of the nanobelt produces elastic energy. The stable shape of the nanobelt is determined by the minimization of the total

RESEARCH ARTICLE

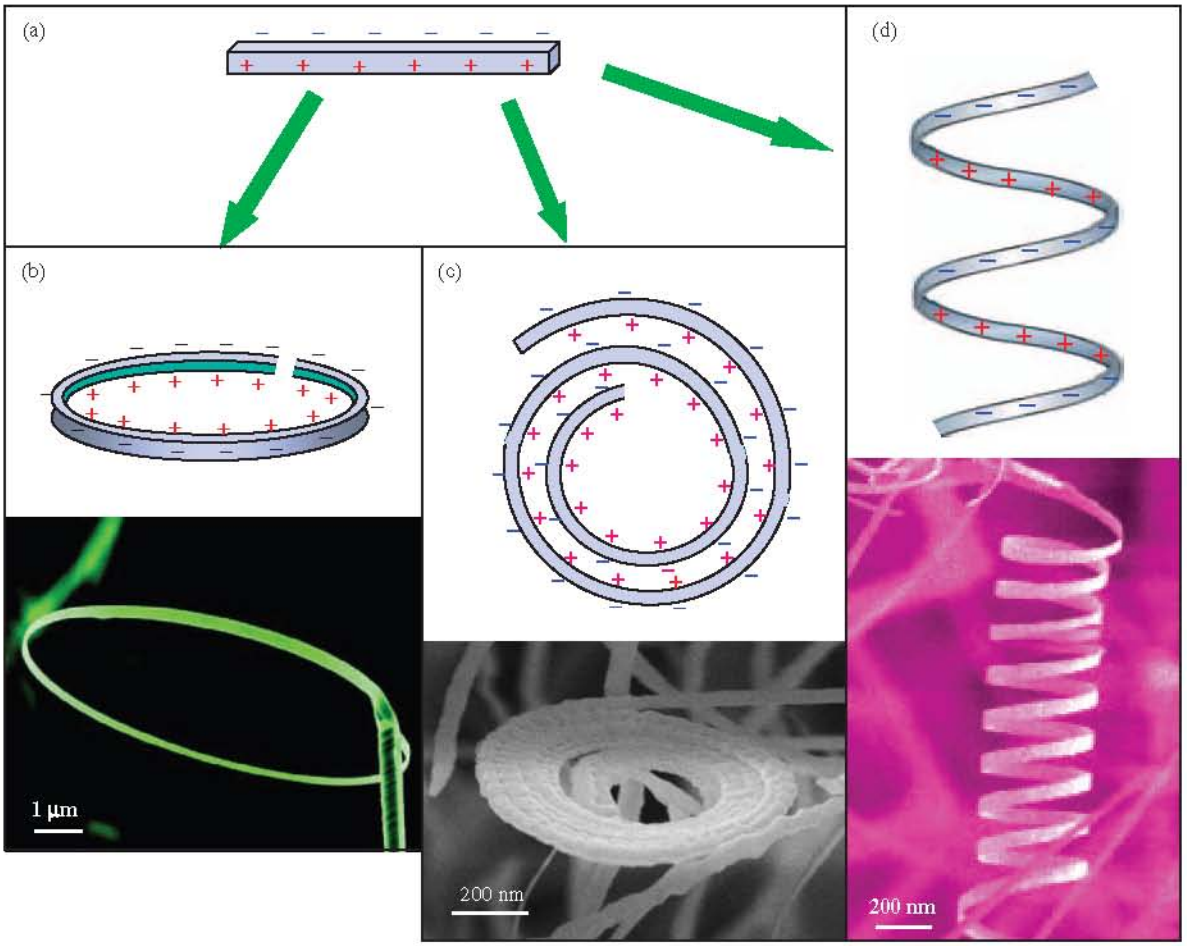

Fig. 9. Nanosprings of piezoelectric nanobelts. (a) A model of the polar surface dominated ZnO nanobelts. (b) Inward bending of the nanobelt results in the formation of a nanoring. (c) The formation of a nano-spiral. (d) The formation of a nanospring.

energy contributed by spontaneous polarization and elasticity. If the nanobelt is rolled loop-by-loop, the repulsive force between the charged surfaces stretches the nanospring, while the elastic deformation force pulls the loops together; the balance between the two forms the nanospring that has elasticity (Fig. 17(d)). The nanospring has a uniform shape with radius of ~500–800 nm and evenly distributed pitches. Each is made of a uniformly deformed single-crystal ZnO nanobelt.

3.2. Seamless Nanorings

By adjusting the raw materials with the introduction of impurities, such as indium, we have synthesized a nanoring structure by the VS process (Fig. 10(a)). The as-synthesized sample is composed of many freestanding nanorings, with typical diameters ~1–4 μm, thin and wide shells of thicknesses ~10–30 nm. SEM images recorded at high-magnification clearly present the perfect circular shape of the complete rings, with uniform shape and flat surfaces. TEM image (Fig. 10(b)) indicates that the nanoring is a single-crystal entity with circular shape, although there is diffraction contrast due to non-uniform deformation along the circumference. The single-crystal structure referred here means a complete nanoring that is made of a single crystalline ribbon bent evenly at the curvature of the nanoring. Electron diffraction pattern recorded from the center of the nanoring shows that the radial direction of the nanoring is $[1\bar{2}10]$, tangential direction $[10\bar{1}0]$ and nanoring axis [0001]. The nanoring is made of co-axial, uni-radius, epitaxial-coiling of a nanobelt. The trace of the coiling nanobelt is seen through the side of the nanoring. The interface between the loops is coherent, epitaxial and chemically bonded. The entire nanoring is a single crystal, although the quality of the crystallinity varies slightly across the width of the nanoring.

The growth of the nanoring structures can be understood from the polar surfaces of the ZnO nanobelt. The polar-nanobelt, which is the building block of the nanoring, grows along $[10\bar{1}0]$, with side surfaces $\pm(1\bar{2}10)$ and top/bottom surfaces $\pm(0001)$, and have a typical width of ~15 nm and thickness ~10 nm. The nanobelt has polar charges on its top and bottom surfaces (Fig. 10(c)). If the surface charges are uncompensated during growth, the nanobelt may tend to fold itself as its length getting longer to minimize the area of the polar surface. One possible

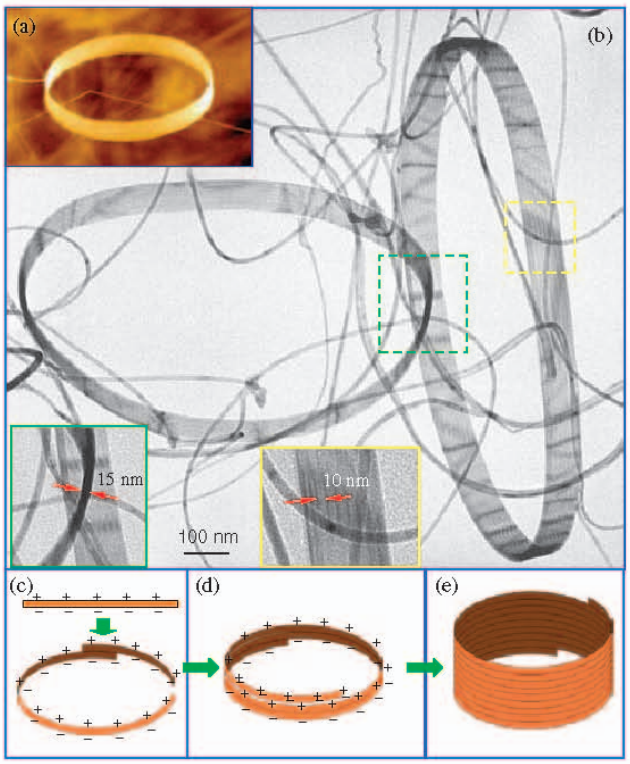

Fig. 10. (a) SEM image of single-crystal seamless nanoring of ZnO. (b) Low magnification TEM image of the ZnO rings and ZnO nanobelts. The nanobelts have uniform shape and their widths are ~15 nm, which is about the same as the thickness of the ring shell, as measured from the tilted image inserted in the figure. The thickness of the nanobelt composing the ring is measured to be 10 nm. (c–e) Proposed growth model showing the initiation and formation of the single-crystal nanoring via self-coiling of a polar nanobelt. The nanoring is initiated by folding a nanobelt into a loop with overlapped ends due to long-range electrostatic interaction among the polar charges; the short-range chemical bonding stabilizes the coiled ring structure; and the spontaneous self-coiling of the nanobelt is driven by minimizing the energy contributed by polar charges, surface area and elastic deformation.

way is to interface the positively charged (0001)-Zn plane (top surface) with the negatively charged (0001)-O plane (bottom surface), resulting in neutralization of the local polar charges and the reduced surface area, thus, forming a loop with an overlapped end (Fig. 10(c)). The radius of the loop may be determined by the initial folding of the nanobelt at the initial growth, but the size of the loop cannot be too small to reduce the elastic deformation energy. The total energy involved in the process comes from polar charges, surface area and elastic deformation. The long-range electrostatic interaction is likely to be the initial driving force for folding the nanobelt to form the first loop for the subsequent growth.

The presence of planar defect within the nanobelt is the key for leading to the fast growth of the nanobelt along $[10\bar{1}0]$, because it lowers the energy in the wurtzite-structured lattice.[77] As the growth continues, the nanobelt may be naturally attracted onto the rim of the nanoring due to electrostatic interaction and extends parallel to the rim of the nanoring to neutralize the local polar charge and reduce the surface area, resulting in the formation of a self-coiled, co-axial, uni-radius, multi-looped nanoring structure (Fig. 10(d)). The self-assembly is spontaneous, which means that the self-coiling along the rim proceeds as the nanobelt grows. The reduced surface area and the formation of chemical bonds (short-range force) between the loops stabilize the coiled structure. The width of the nanoring increases as more loops winding along the nanoring axis, and all of them remain in the same crystal orientation. Since the growth was carried out in a temperature region of 200–400 °C, "epitaxial sintering" of the adjacent loops forms a single-crystal cylindrical nanoring structure, and the loops of the nanobelt are joined by chemical bonds as a single entity (Fig. 10(e)). A uni-radius and perfectly aligned coiling is energetically favorable because of the complete neutralization of the local polar charges inside the nanoring and the reduced surface area. Theoretical calculation shows consistent result.

Ring structure is of great interest to physical science and technological applications. The Aharonov-Bohm effect about interference phenomena of electrons has been investigated for gold rings[78] and superconducting Nb rings.[79] Persistent current in a metal ring threaded by a magnetic flux was investigated.[80] Carbon nanotube rings,[81,82] $NbSe_3$ rings[83] and Möbius strips[84] have been reported. The polar-charge induced nanorings presented here are unique and distinct, and have potential applications in investigating fundamental physical phenomena, such as the Aharonov-Bohm oscillations in the exciton luminescence.[85] The unique piezoelectric and semiconducting properties of ZnO predict that the nanorings could be nano-scale sensors, transducers and resonators.

3.3. Effect from Growth Kinetics

It is a common fact that the {0001} polar surfaces are the dominant facets of single-crystal nanosprings and nanoloops of ZnO. Since the polar surfaces {0001} have higher surface energy than either $\{2\bar{1}\bar{1}0\}$ or $\{10\bar{1}0\}$, finding experimental conditions that make it possible for forming the higher energy {0001} surface is the key. To find a clue, Table II summarizes the experimental conditions, growth morphology and dominant surfaces of ZnO nanostructures. It is shown that, despite the source peak temperature in the range of 1300–1400 °C and a variation in vaporization time, unanimously both polar surfaces dominated and non-polar surface dominated nanobelts could be produced. In the column of source materials used, it is clearly seen that polar surface dominated nanobelts were synthesized with or without doping in ZnO. The pressure of the gas flow appears also not critical to the formation of polar surfaces unless the pressure becomes very low.[86] A common and striking fact is that a pre-evacuation of the growth chamber to $\sim 10^{-3}$ torr appears to be necessary for growing {0001} dominated nanobelts. It is suggested a pre-pumping would

RESEARCH ARTICLE

Table II. A summary of the ZnO belt-like nanostructures synthesized by a vapor-solid process.

	Nanobelt growth direction/dominant flat surfaces	Yield (%)	Peak Temperature(°C); time at peak temperature; source materials	Flow rate of Ar gas (sccm)	Pre-growth pressure; pressure during growth (mbar)
Nanobelts	[0001]/{10-10}; or [10-10]/{2-1-10}	100	1400 °C; 120 min; ZnO	50	400; 400
Nanosprings and nanorings	[2-1-10]/{0001}	~5	1350 °C; 30 min; ZnO:Li_2O	25	$\sim 10^{-3}$; 330
Nanorings	[10-10]/{0001}	~20	1400 °C; 30 min; ZnO:In_2O_3:Li_2CO_3	50	$\sim 10^{-3}$; 660
Nanobows	[10-10]/{0001}	5	1350 °C; 120 min; ~10 hrs; ZnO	50	$\sim 10^{-2}$; 300
Nanosprings (current work)	[2-1-10]/{0001}	50–100	1390 °C; 120–360 min; ZnO	50	$\sim 10^{-3}$; 250–300
Nanorings and nanospirals (current work)	[10-10]/{0001}	20	1390 °C; 120–360 min; ZnO	50	$\sim 10^{-3}$; 250–300

* The pressure in the growth chamber was quickly dropped to ~0.1 mbar towards the end of the growth.

reduce the content of oxygen and other gas species in the growth chamber, thus, greatly reduces the possibility of molecular adsorption on the {0001} polar surfaces. This step appears to be the key for high-yield growth of polar surface dominated nanostructures. In the current work, the synthesis was conducted at 1390 °C for 2~6 hours under a confined pressure range of 250~300 mbar after the temperature of reaction chamber was ramped to 800 °C, where argon carrier gas was kept with a flow rate of 50 sccm throughout the high-temperature synthesis and cooling processes. Before inletting argon carrier gas, the pre-growth pressure of 2×10^{-2} torr was maintained for 3 to 8 hours.

In a separated experiment, we have found that a sudden drop in chamber pressure can also lead to formation of polar surface dominated nanobows.[23] At a growth chamber pressure of 300 mbar, [0001] ZnO nanowires were grown (Fig. 11). A sudden decrease of the chamber pressure to 0.1 mbar results in the formation of nanorings and nanobows at the growth front, which were formed by rolling the *c*-plane dominated nanobelts. A drop in pressure may be favorable of formation of polar surfaces due to the reduced probability of foreign molecule adsorption on the surface to neutralize the polar charges. The polar nanobelts, responsible for the formation of nanorings and nanobows, grow along either the $[2\bar{1}\bar{1}0]$ or $[01\bar{1}0]$ direction. A ring is formed by folding a polar nanobelt so that its *c*-axis points to the center of the ring. A change in growth direction from $[01\bar{1}0]/[2\bar{1}\bar{1}0]$ to $[10\bar{1}0]/[\bar{1}2\bar{1}0]$ could result in the formation of two crossed rings at 60° angle.

3.4. Self-Catalyzed Growth Structures

Asymmetric crystal structure of a material may introduce anisotropic growth structure. As we have shown for ZnO, the (0001) surface is terminated with Zn, and the $(000\bar{1})$ surface is terminated with O. The former is catalytically active, while the latter is relatively inert, possibly resulting in anisotropic growth phenomena. In this section, we use the formations of nanocombs and tetrapoles as examples to illustrate the self-catalysis effect.

"Comb-like" structures have been observed for wurtzite structured materials, such as ZnO,[87] ZnS,[88] and CdSe.[89] The comb structures (Figs. 12(a, b)) are ZnO and have the comb-teeth growing along [0001], the top/bottom surfaces being $\pm(01\bar{1}0)$, and side surfaces $\pm(2\bar{1}\bar{1}0)$. Using convergent beam electron diffraction (CBED),[90] which relies on dynamic scattering effect and is an effective technique for determining the polarity of wurtzite structure, we have found that the comb structure is an asymmetric growth along Zn-[0001] (Fig. 33(b)).[91] This conclusion is received by comparison the experimentally observed CBED pattern and the theoretically calculated pattern by matching the fine detailed structure features in the (0002) and $(000\bar{2})$ diffraction disks (Figs. 12(d and e)). The positively charged Zn-(0001) surface is chemically active and the negatively charged O-$(000\bar{1})$ surface is relatively inert, resulting in a growth of long fingers along [0001]. Using HRTEM, we found that the Zn-terminated (0001) surface has tiny Zn clusters, which could lead to self-catalyzed growth without the presence of foreign catalyst.[91] The chemically inactive $(000\bar{1})$ surface typically does not grow nanobelt structure.

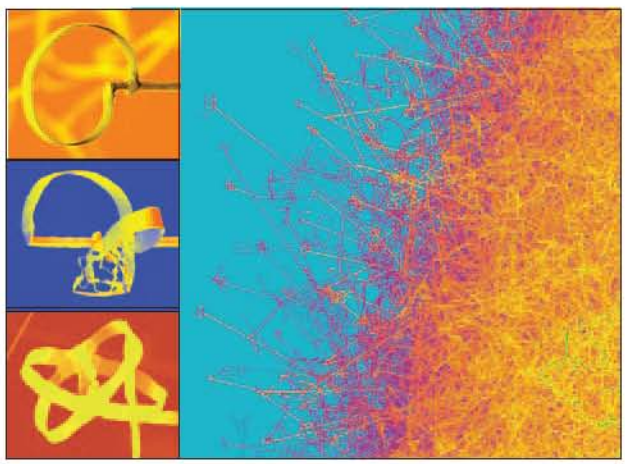

Fig. 11. Controlled growth of nanorings and nanobows at the tips of ZnO nanorods/nanowires by a sudden change in growth pressure towards the end of the experiment, so that the grow direction switched from [0001] to $[01\bar{1}0]$ or $[2\bar{1}\bar{1}0]$. The polar surface dominated nanobelts bent to form nanorings and nanobows.

RESEARCH ARTICLE

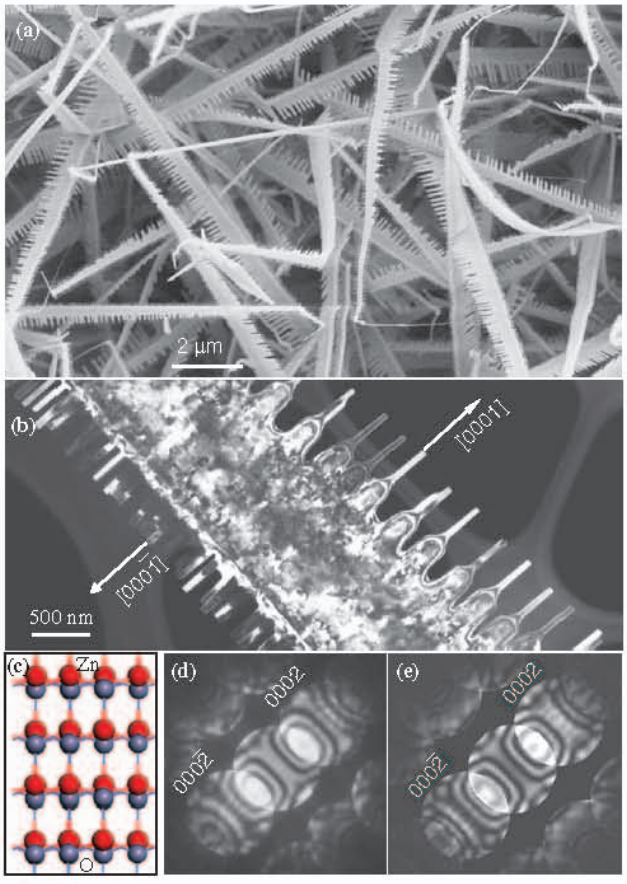

Fig. 12. Self-catalyzed growth of cation terminated polar surfaces. (a) SEM image of "comb-like" cantilever arrays of ZnO, which is the result of surface polarization induced growth due to the chemically active (0001)-Zn. (b) High-resolution TEM recorded from the tip of the comb-teeth, showing possible evidence of Zn segregation at the growth front, which is likely to be effective for driving self-catalyzed growth. (c) Structure model of ZnO projected along [01$\bar{1}$0], showing the termination effect of the crystal. (d, e) Experimentally observed and theoretically simulated convergent beam electron diffraction patterns for determining the polarity of the nanocombs, respectively.

4. COMPOSITE-HYDROXIDE-MEDIATED APPROACH FOR THE SYNTHESIS OF NANOSTRUCTURES OF COMPLEX FUNCTIONAL-OXIDES

Complex oxides with structures such as perovskite, spinel, and garnet have many important properties and applications in science and engineering, such as ferroelectricity, ferromagnetism, colossal magnetoresistance, semiconductor, luminance, and optoelectronics.[92–97] Synthesizing nanostructures of complex oxides is rather challenging because of difficulties in controlling the composition, stoichiometry and/or crystal structure. The existing techniques rely on high pressure, salt-solvent mediated high temperature, surface capping agent, or organometallic precursor mediated growth process[98–107] and the types of oxides that can be synthesized are limited. We have reported a general and widely applicable approach for synthesis of complex oxide nanostructures of scientific and technological importance.[108] The method is based on a reaction between a metallic salt and a metallic oxide in a solution of molten mixed potassium hydroxide and sodium hydroxide eutectic at ~200 °C and normal atmosphere without using organic dispersant or capping agent. This methodology provides a one-step, convenient, low cost, nontoxic and mass-production route for synthesis of nanostructures of functional oxide materials of various structure types.

We now use the synthesis of two families of complex oxides, perovskite (ABO_3; $A_xA'_{1-x}BO_3$; $AB_xB'_{1-x}O_3$) and spinel (AB_2O_4), to illustrate the principle and applications of the approach. The sources for A and A' cations are from metallic salts, such as nitrates, chlorates, or acetates, and the sources for B and B' cations are from oxides with valence states that match to those present in the desired product to be synthesized. The mixed-hydroxides is used to not only mediate the reactions between the raw materials containing A (A') and B (B') cations, but also low the reaction temperature to ~200 °C or even less. A total of 8 examples are selected here for illustrating this generalized approach.

Our first example is $BaTiO_3$, an important ferroelectric material. The synthesis follows the following steps.[109]

(i) An amount of 20 g of mixed hydroxides (NaOH:KOH = 51.5:48.5) (MHDs) was placed in a 25 ml Teflon vessel with a cover for preventing dust.

(ii) A mixture of anhydrous $BaCl_2$ and TiO_2 at 0.5 mmol each was used as the raw material for reaction.

(iii) The raw material was placed on the top of the hydroxide in the vessel. The vessel was put in a furnace, which was preheated to 200 °C.

(iv) After the hydroxides being totally molten, the hydroxide solution was stirred by a platinum bar or by shaking the covered vessel to ensure the uniformly of the mixed reactants.

(v) After reacting for 48 hours, the vessel was taken out and cooled down to room temperature.

Deionized water was added to the solid product. The product was filtered and washed by first deionized water and then hot water to remove hydroxide on the surface of the particles. The synthesized product was received. For the next seven types of materials to be presented, all of the synthesis procedures are the same as stated above except replacing the raw materials in Step (ii).

X-ray diffraction (XRD) measurement proved that the as-synthesized product is tetragonal $BaTiO_3$ (P4mm, JCPD 81-2203) (Fig. 13(a)). Scanning electron microscopy (SEM) image of the powder shows that the particles are nanocubes or nanocuboids with 30–50 nm in sizes (Fig. 13(b)), and energy dispersive X-ray analysis (EDS) shows the presence of oxygen, barium, and titanium. Electron diffraction (ED) and high-resolution transmission electron microscope (HRTEM) images show that the nanocubes are single crystal and the three crystal faces are {100} planes (Fig. 13(c) and insert).

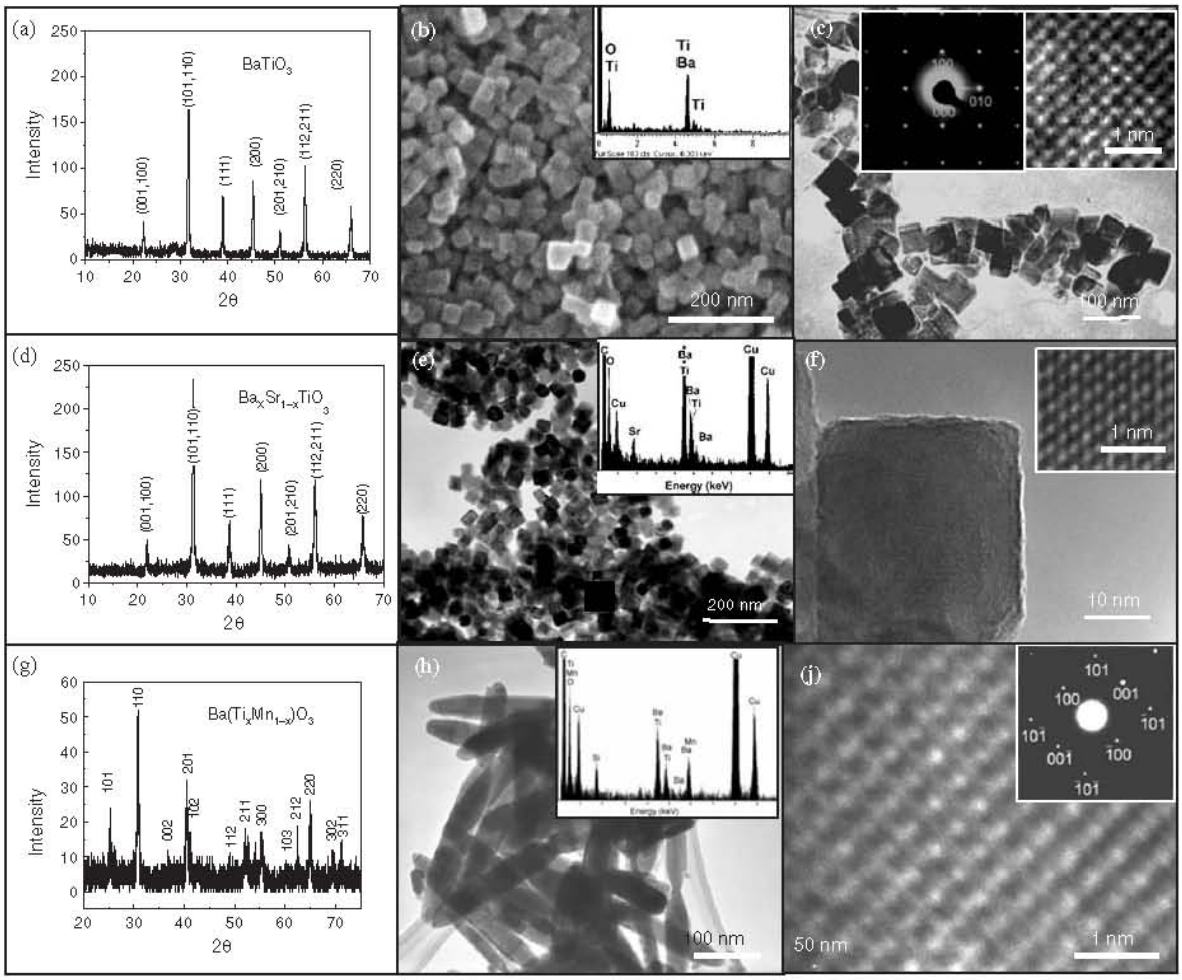

Fig. 13. Perovskite (a–c) $BaTiO_3$ and (d–f) $Ba_xSr_{1-x}TiO_3$ nanocubes and (g–j) $Ba(Ti_xMn_{1-x})O_3$ synthesized by the composite-hydroxide mediated approach. (a) XRD pattern of $BaTiO_3$ nanopowder. (b) SEM image of $BaTiO_3$ nanocubes; insert is EDS of the nanocubes showing the presence of Ba, Ti and O. (c) TEM image of $BaTiO_3$ nanocubes, inserts are electron diffraction pattern and HRTEM image of a nanocube, showing its single-crystal structure. (d) XRD pattern of $Ba_xSr_{1-x}TiO_3$ nanopowder. (e) TEM image of $Ba_xSr_{1-x}TiO_3$ nanopowder; insert is EDS of the nanocubes showing the presence of Ba, Sr, Ti and O. The Cu signal came from the TEM grid. (f) A single-crystal $Ba_xSr_{1-x}TiO_3$ nanocube and its corresponding HRTEM image (insert). (g) XRD pattern of $BaTi_xMn_{1-x}O_3$ nanopowder. (h) TEM image of the nanostructure. (i) A single-crystal nanostructure and (j) its HRTEM image as well as its electron diffraction pattern (insert).

From the above experimental results, a possible reaction mechanism for the synthesis of $BaTiO_3$ in hydroxide solution is suggested as following. Although the molting points of both pure sodium hydroxide and potassium hydroxide are over 300 °C, $T_m = 323$ °C for NaOH, and $T_m = 360$ °C for KOH, the eutectic point at NaOH/KOH = 51.5:48.5 is only about 165 °C (Fig. 14). This is likely the key for synthesizing the complex oxide at ~200 °C or lower. During the reaction process, hydroxides play a role not only as a solvent, but also as a reactant for lowing the reaction temperature. In the molten hydroxide, TiO_2 reacts with NaOH/KOH and forms a hydroxide-soluble Na_2TiO_3/K_2TiO_3. To simplify the expression for chemical reactions here and after, we only include NaOH in the formula for simplicity:

$$2NaOH + TiO_2 \rightarrow Na_2TiO_3 + H_2O \qquad (5)$$

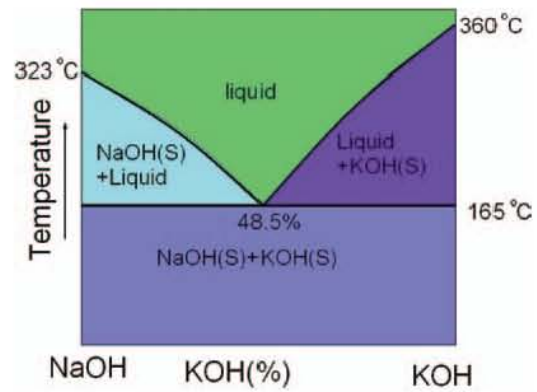

Fig. 14. Phase diagram of NaOH-KOH. Molting points of potassium hydroxide is 323 °C. Molting point of sodium hydroxide is 360 °C. The eutectic point at NaOH/KOH = 51.5:48.5 is only about 165 °C.

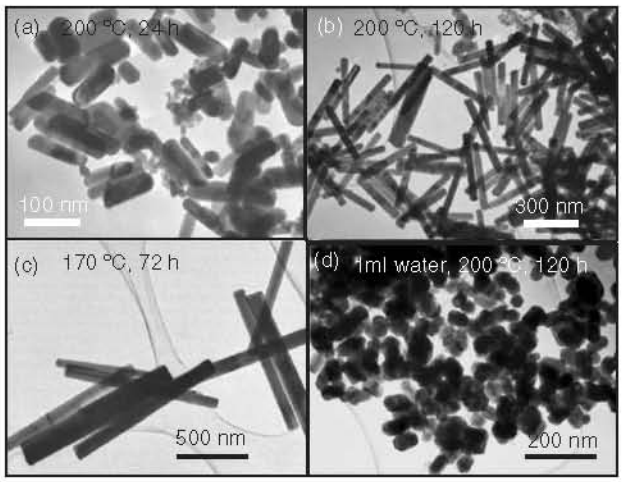

Fig. 15. TEM images of $BaMnO_3$ grown by the composite-hydroxide mediated approach at different time and temperature. (a) at 200 °C for 24 hours, (b) at 200 °C for 120 hours, (c) at 170 °C for 72 hours and (d) at 200 °C for 120 hours, adding 1 ml water.

At the same time, $BaCl_2$ reacts with hydroxide to form $Ba(OH)_2$, which is dissolved in the hydroxide solution:

$$BaCl_2 + 2NaOH \rightarrow Ba(OH)_2 + 2NaCl \quad (6)$$

The Na_2TiO_3 from process (5) reacts with $Ba(OH)_2$ produced in process (6) and forms an indissoluble solid $BaTiO_3$:

$$Na_2TiO_3 + Ba(OH)_2 \rightarrow BaTiO_3 + 2NaOH \quad (7)$$

The Gibbs free energy following the above three steps for the formation of $BaTiO_3$ at 200 °C is calculated to be −24.16 Kcal/mol.[110] Because the viscosity of hydroxide is large, the formation of $BaTiO_3$ nanostructure is slow and it is not easy for the nanostructures to agglomerate. This is likely the key for receiving dispersive single crystalline nanostructures during the reaction without using organic surface capping material. The hydroxides mediate the reaction, but they are not part of the final nanostructures.

The second example, $Ba_{0.5}Sr_{0.5}TiO_3$ was synthesized to explore the applicability of this method for synthesis of complex perovskites. Following the same procedures as used for receiving $BaTiO_3$ except replacing the raw cation supplying materials by a mixture of $BaCl_2$, $SrCl_2$ and TiO_2 at 0.5, 0.5 and 1.0 mmol, respectively. XRD pattern shows that the received product is a pure perovskite $Ba_{0.5}Sr_{0.5}TiO_3$ phase (Fig. 13(d)). TEM measurement demonstrated that the powder product is nanocubes with about 30–40 nm in sizes (Fig. 13(e)). EDS measurement shows that the ratio of the elements in the product is Ba:Sr:Ti = 1:1:2, demonstrating the controllability in chemical composition. HRTEM observation proved that $Ba_{0.5}Sr_{0.5}TiO_3$ nanocubes are single crystals (Fig. 13(f) and insert). However, there are some defects and atomic disorders in the crystal because strontium and barium share the same sites in the crystal, which possibly results in substitutional point defects. For both of $BaTiO_3$ and $Ba_{0.5}Sr_{0.5}TiO_3$, the crystal face is clean and sharp, and no amorphous layer is present, because no organic reagent or capping material was introduced during the synthesis. The perovskite nanocubes with clean surfaces are desirable for investigating ferroelectricity at nano-scale and for building functional components. Figures 13(g–h) are the results of $Ba(Ti, Mn)O_3$.

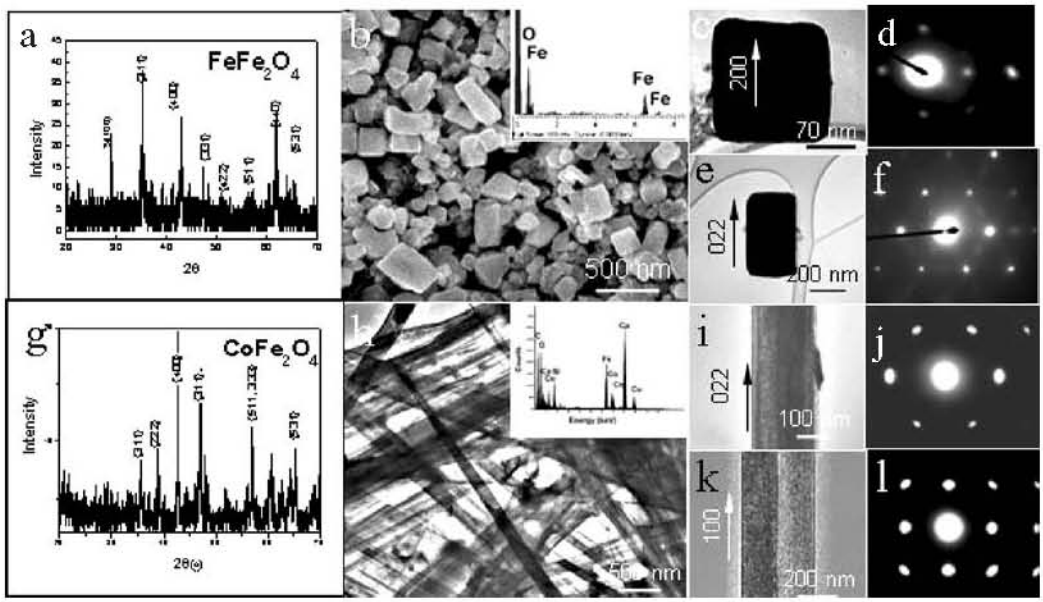

Fig. 16. Spinel (a–f) Fe_3O_4 nanoparticles and (g–l) $CoFe_2O_4$ nanobelts synthesized by the composite-hydroxide mediated approach. (a) XRD pattern of Fe_3O_4; (b) SEM image of Fe_3O_4 nanoparticles, and EDS pattern (insert). (c) A cube-like nanoparticle and (d) its electron diffraction pattern. (e) A Fe_3O_4 cuboids and (f) its diffraction pattern. (g) XRD pattern of $CoFe_2O_4$ nanobelts. (h) Morphology of the nanobelts and the corresponding EDS spectrum (insert) showing the presence of Co, Fe and O. The Si signal came from the TEM grid and holder. (i) A single-crystal nanobelt growing along [121] and (j) its electron diffraction pattern. (k) A nanobelt growing along [100] and (l) its electron diffraction pattern.

RESEARCH ARTICLE

The morphology of the oxide nanobelts can be tuned by varying the length of reaction time. Figure 15 shows the four configuration of $BaTiO_3$ nanobelts received by controlling the reaction time. This experiment demonstrate the high tunability of the synthesis process.

Ferromagnetic spinel structured complex oxide was chose as the third example to demonstrate the extensive applicability of the synthesis method. To synthesize spinel Fe_3O_4 ($Fe^{2+}Fe_2^{3+}O_4$) nanostructure, a mixture of anhydrous $FeCl_2$ and Fe_2O_3 at 0.5 mmol each was used as the raw material for providing Fe^{2+} and Fe^{3+} cations at the desired atomic ratio. Synthesis temperature and time were 200 °C and 72 hours, respectively. XRD and EDS show that the product is cubic Fe_3O_4 (JCPDS 89-3854) (Fig. 16(a) and insert in Fig. 16(b)). In the product, most particles are nanocubes about 250 nm in sizes, and nanocuboids about 250 nm in short sides and 300–400 nm in long sides. From ED patterns of single particles, we can see that the nanocubes and nanocuboids are single crystals. The faces of the nanocubes are the {100} crystallographic planes (Figs. 16(c and d)). The growth direction of the nanocuboids is [121] (Figs. 16(e and f)).

$CoFe_2O_4$ nanocrystals were synthesized as the fourth example. A mixture of $Co(NO_3)_2 \cdot 6H_2O$ and Fe_2O_3 at 0.5 mmol each was used as the raw material. XRD pattern demonstrated that the product is cubic $CoFe_2O_4$ (JCPDS 22-1086) (Fig. 16(g)), as supported by EDS microanalysis (insert in Fig. 16(h)). The morphology of $CoFe_2O_4$ is nanobelts with about 20–40 nm in thickness, 150–250 in width, and more than 20 μm in length (Fig. 16(h)). ED shows that there are two kinds of belts growing along different directions, [121] and [100] (Figs. 16(i, j, k and l)). The suggested formation mechanism of ferromagnetic MFe_2O_4 (M = Co, Fe, Ni, Co) spinel nanostructures is as following:

$$MCl_2 + 2NaOH \rightarrow M(OH)_2 + 2NaCl;$$

$$\text{or} \quad M(NO_3)_2 + 2NaOH \rightarrow M(OH)_2 + 2NaNO_3 \quad (8)$$

$$Fe_2O_3 + NaOH \rightarrow Na_2Fe_2O_4 + H_2O \quad (9)$$

$$M(OH)_2 + Na_2Fe_2O_4 \rightarrow MFe_2O_4 + 2NaOH \quad (10)$$

5. FUNDAMENTAL PROPERTIES OF NANOWIRES AND NANOBELTS

The availability of a wide range of oxide NW and NB materials with controlled chemical composition, physical size and electronic properties opens up many exciting opportunities ranging from fundamental studies of the role of dimensionality on physical properties to potential applications in nanoscale optoelectronics, sensors, actuators and other areas. In the section, we will introduce some measurement techniques for quantifying the mechanical, field emission, thermal, electrical and optical properties of individual NW structures.

5.1. Mechanical Properties of Nanobelts and Nanowires

5.1.1. *In-Situ Resonance of a Nanobelt*

Atomic force microscopy (AFM) is powerful in characterizing the mechanical properties of nanostructures. Using the tip of an AFM to deflect a carbon nanotube, the displacement of the nanotube is directly related to the force acting on the tip, from which the Young's modulus of a carbon nanotube was measured.[111] Based on the electric-field-induced resonant excitation, an alternative technique has been developed for measuring the mechanical properties of individual nanowire-like structures by *in situ* transmission electron microscopy (TEM).[112, 113] Using this method, Mechanical properties of carbon nanotubes,[112, 114] silicon nanowires,[115] and silicon carbide-silica composite nanowires[115] have been quantified.

To carry out the mechanical property measurements of a nanobelt, a specimen holder for a Hitachi HF-2000 TEM (200 kV) was built for applying a voltage across a nanobelt and its counter electrode. Mechanical resonance can be induced if the applied frequency matches the natural resonance frequency of the nanobelt. Due to the mirror symmetry of the nanobelt (Fig. 17(a)), there are two distinct fundamental resonance frequencies corresponding to the vibration in the thickness and width directions, which are given from the classical elasticity theory as[116]

$$\nu_x = \frac{\beta_1^2 T}{4\pi L^2}\sqrt{\frac{E_x}{3\rho}} \quad (11)$$

$$\nu_y = \frac{\beta_1^2 W}{4\pi L^2}\sqrt{\frac{E_y}{3\rho}} \quad (12)$$

where $\beta_1 = 1.875$ for the first harmonic resonance; E_x and E_y are the bending modulus if the vibration is along x-axis (thickness direction) and y direction (width direction), respectively; ρ is the density, L is the length, W is the width and T is the thickness of the nanobelt. The two modes are decoupled and they can be observed separately in experiments.

Changing the frequency of the applied voltage, we found two fundamental frequencies in two orthogonal directions transverse to the nanobelt.[117] Figures 17(b and c) show the harmonic resonance with the vibration planes nearly perpendicular and parallel to the viewing direction, respectively. For calculating the bending modulus, it is critical to accurately measure the fundamental resonance frequency (ν_1) and the dimensional sizes (L and T or W) of the investigated ZnO nanobelts. To determine ν_1, we have checked the stability of resonance frequency to ensure one end of nanobelt is tightly fixed, and the resonant excitation have been carefully checked around the half value of the resonance frequency. The specimen holder can be rotated about its axis so that the nanobelt can

RESEARCH ARTICLE

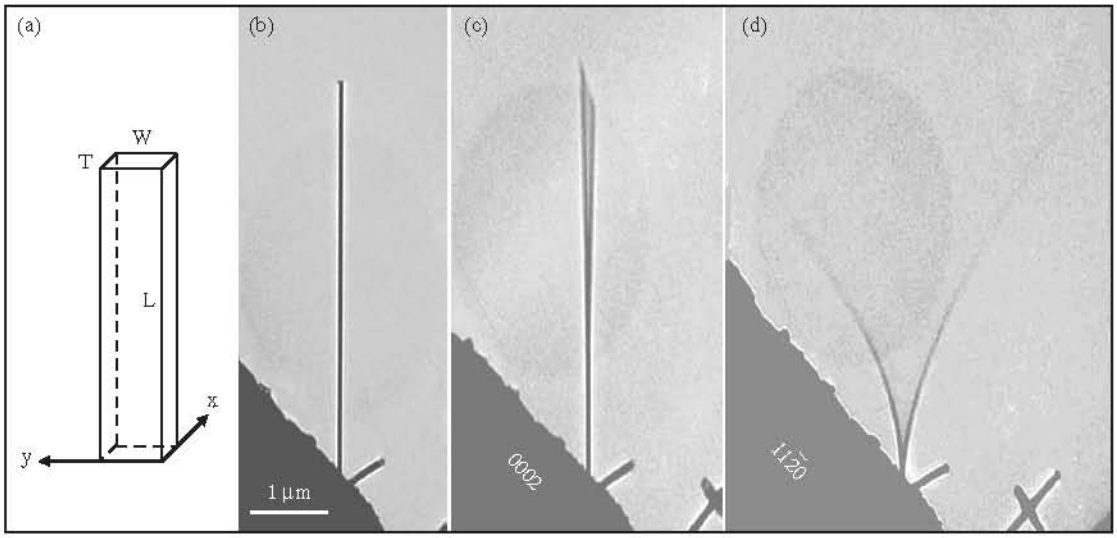

Fig. 17. Measuring the bending modulus of a nanobelt. (a) Geometrical shape of a nanobelt. (b) A ZnO nanobelt at stationary. (c, d) Mechanical resonance of the nanobelt along two orthogonal directions, respectively, closely perpendicular to the viewing direction ($\nu_x = 622$ KHz), and nearly parallel to the viewing direction ($\nu_y = 691$ KHz).

be aligned perpendicular to the electron beam, so the real length (L) of the nanobelt can be measured. The projection direction along the beam is determined by electron diffraction pattern, so that the true thickness and width can be determined because the normal direction of the nanobelt is $[2\bar{1}\bar{1}0]$. Based on the experimental data, the bending moduli of the ZnO nanobelts can be calculated using Eqs. (11) or (12).[117] The bending modulus of the ZnO nanobelts was ~52 GPa. Our experiments clearly shows that the nanobelt can be effective nanoresonators exhibiting two orthogonal resonance modes, which can be used as probes for SPM operated in tapping and scanning modes.

5.1.2. *Mechanical Behavior of Aligned Nanowire Array*

For the aligned ZnO NWs, we have recently demonstrated an AFM based technique for measuring the elastic properties of individual ZnO NW without destructing the specimen.[118] By simultaneously recording the topography and lateral force image in AFM contact mode when the AFM tip scans across the aligned nanowire arrays, the elastic modulus of individual NWs is determined. This technique allows a measurement of the mechanical properties of individual NWs of different lengths in an aligned array without destructing or manipulating the sample.

The principle for the AFM measurement is illustrated in Figure 18(a). In AFM contact mode, a constant normal force is kept between the tip and sample surface. The tip scans over the top of the ZnO NW and the tip's height is adjusted according to the surface morphology and local contacting force. Before the tip meets a NW, a small lateral force is observed (Fig. 18(a)-I). When the tip comes in contact with a NW, the lateral force increases almost linearly as the NW is elastically bent from its equilibrium position (Fig. 18(a)-II and III). At the largest bending position, as illustrated in Figure 18(d), the tip crosses the top of the NW, then the NW is released; the lateral force drops suddenly and reaches the ordinary level (Fig. 18(a)-V).

The elastic modulus is derived based on the following calculation. From the geometrical relationship illustrated in Figure 6(a)-IV, when a vertical NW experiences a lateral force f parallel to the scanning direction, the force f can be expressed as:

$$f = 3EI\frac{x}{L^3} \tag{13}$$

where E and I are the elastic modulus and momentum of inertia of the NW, x is the lateral displacement perpendicular to the NW, and L is the length of the NW. From Hook's law, the spring constant is $K = f/x$. For a ZnO NW with a hexagonal cross-section, its momentum of inertia is $I = (5(3^{1/2})/16)a^4$, where a is the radius of the NW. Therefore, the elastic modulus is given by:

$$E = \frac{16L^3K}{15\sqrt{3}a^4} \tag{14}$$

The displacement and the lateral force were determined from the topography image and the corresponding lateral force image, as shown in Figures 18(b and c), respectively. To ensure that the center of the conical tip touches the center of the NW as assumed in theoretical calculation, both curves were read from the center of the NW as indicated in the images by dashed lines. Taking a line scan across the middle point of a spot in the topography image, a curve for the scanner retracting distance ~~verses~~ the NW lateral displacement was obtained, as shown in Figure 18(d). Likewise, the maximum maximal lateral

RESEARCH ARTICLE

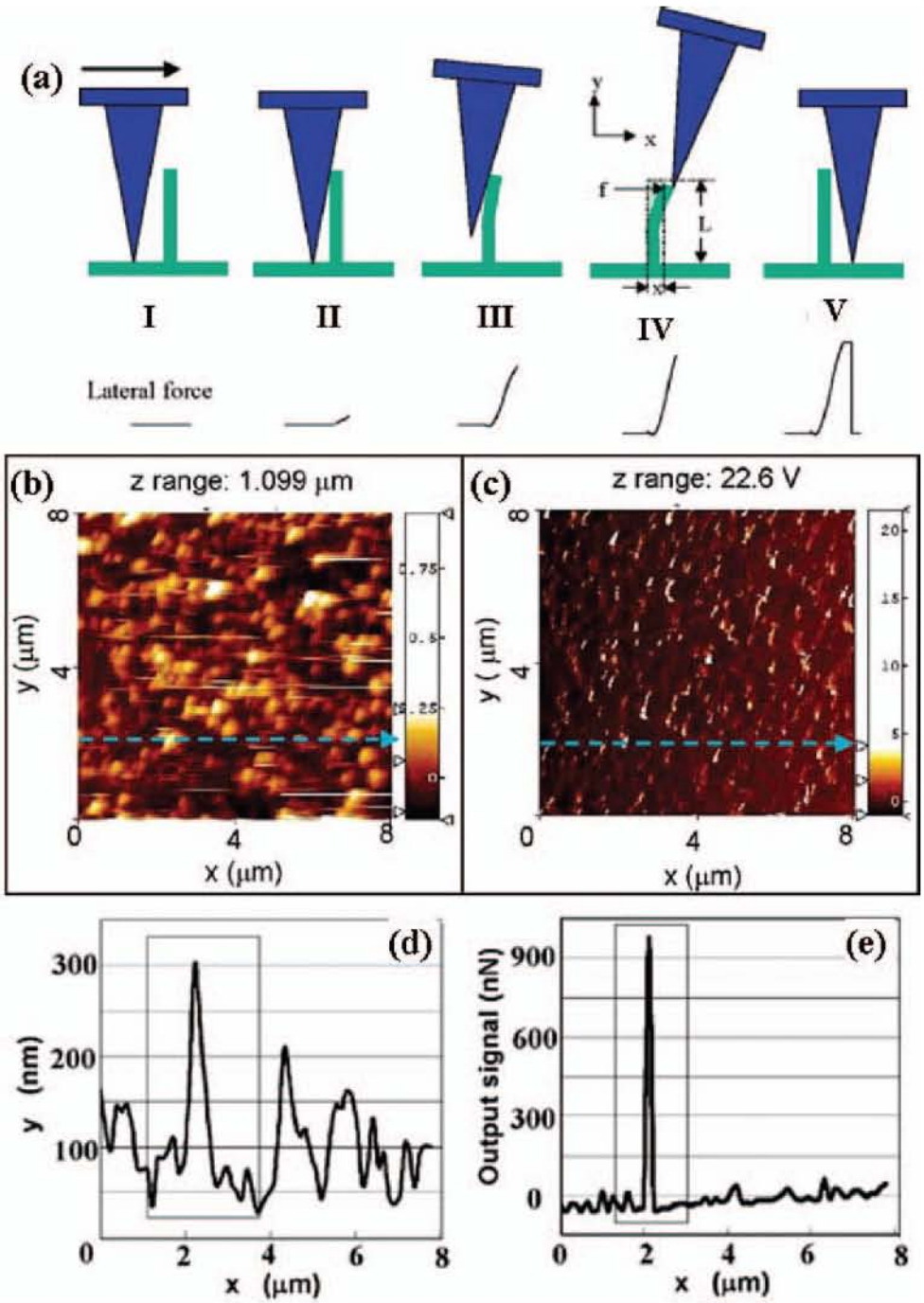

Fig. 18. (a) Procedures for measuring the elastic modulus of aligned nanowire arrays in the AFM contacting mode. (b) Topography image and (c) lateral force image of the aligned ZnO NWs received in AFM contacting mode. (d, e) Line scanning profile along the dashed lines in b and c, respectively.

force for bending the NW was measured by taking a scanning profile at the corresponding line in the lateral force image (as indicated in Fig. 2(e)). Combining the measured x_m and f_m from the two line profiles, the spring constant $K = f_m/x_m$ was obtained. For the ZnO nanowires grown on sapphire surfaces with an average diameter of 45 nm, the elastic modulus was determined to be 29 ± 8 GPa. This technique provided a direct observation on the mechanical properties of aligned NWs, which is of great importance for their applications in electronics, optoelectronics, sensors, and actuators.

5.1.3. *Mechanical Properties of Bridged Nanobelt*

Atomic force microscopy (AFM) is a common technique for characterizing the mechanical behavior of

nanostructures.[119, 120] One of the most important strategies is deforming a NW that is supported at the two ends using an AFM tip, which pushes the NW at its middle point. Quantifying the middle-point force-displacement curve gives the elastic modulus. The accuracy of this measurement is, however, limited by the size of the tip and the accuracy of positioning the AFM tip right at the middle of the 1D nanostructure due to the unavoidable hysteresis of the piezoceramic actuator of the AFM cantilever. We have demonstrated a new approach for quantifying the elastic deformation behavior of a NW by fitting the image profile measured using atomic force microscopy (AFM) in contact mode along the entire length of a bridged/suspended NB/NW/ nanotube under different load forces (Fig. 19(a)).[121] The profile images of the NB recorded the deformation of all of the points along its length under different applied forces (Fig. 19(b)).

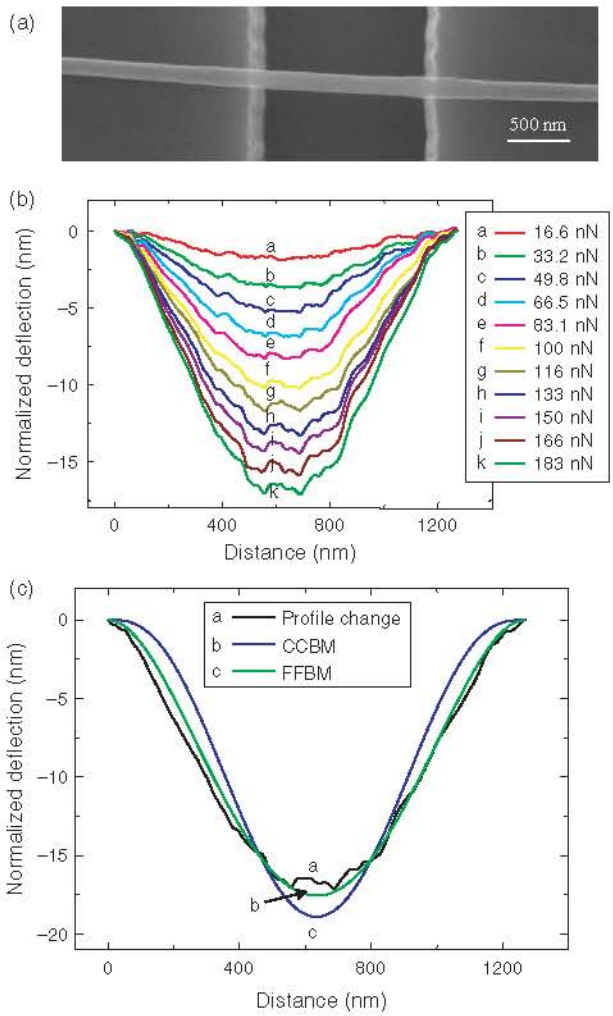

Fig. 19. (a) SEM image of one NB bridged over a trench. (b) The normalized AFM image profile after removing the surface roughness by subtracting the curve acquired at 106 nN; the force is also normalized in reference to the "zero setting point" of 106 nN. (c) Curve fitting using the CCBM and FFBM for the image profiles of NB 1 acquired under normalized force of 183 nN.

One profile could contain up to 650 points, and each point on the suspended portion of NB in the images can be regarded as a mechanical measurement. Consistently fitting the measured deformation profiles can uniquely determine if the measured data are best fit by either the clamped-clamped beam model (CCBM) or the free-free beam model (FFBM) without pre-assumption (Fig. 19(c)), and it eliminates the uncertainty in defining the central point of the suspended beam, thus, greatly increased the precision and reliability of the measurement for elastic modulus.

5.2. Field Emission Properties

5.2.1. Emission Characteristics of Aligned Nanowires

The sharp geometrical shape of nanotubes and nanowires indicates that they might be ideal object for superior field emission. The growth of aligned nanotubes and nanowires has stimulated a great interest in exploring the applications of 1D nanostructure for field emission. The unique geometrical shape of nanobelts is ideal for field emission. Nanowires of refractory materials[122, 123] are potential candidates for field emission applications.

In this section, we use aligned Mo, MoO_2 and MoO_3 nanowires as examples to illustrate the field emission characteristics of NWs.[124] The NW arrays were grown by a solid vaporization of metal powders (see the SEM image shown in Fig. 20). The field emission measurements were carried out in a vacuum chamber of $\sim 2.0 \times 10^{-7}$ Torr at room temperature. The nanowire arrays were first adhered using silver paint to the surface of an oxygen-free high conductivity copper. A transparent anode consists of a quartz plate of 4 cm in diameter coated with conducting tin oxide film was placed in front of and parallel to the surface of the sample cathode. Figure 20 shows the plots

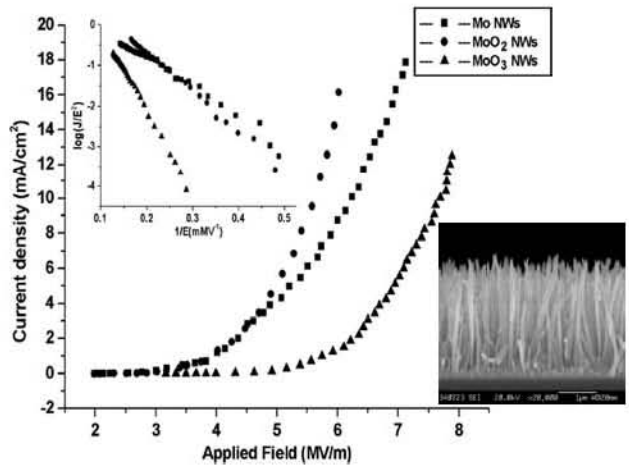

Fig. 20. Field emission current versus electric field (I–E) plots of the Mo, MoO_2 and MoO_3 nanowire arrays and their corresponding F-N plots (inset). The SEM image on right-hand side is aligned Mo nanowires (courtesy of Dr. Jun Zhou and Prof. N. S. Xue, Zhongshan University).

RESEARCH ARTICLE

of field emission current versus applied electric field of the metallic Mo, MoO_2 and MoO_3 nanowire arrays. We determined from the plots their field emission turn-on field (E_{to}) and threshold field (E_{thr}), which are defined to be the macroscopic fields required to produce a current density of 10 μA/cm^2 and 10 mA/cm^2, respectively. The E_{thr} of Mo, MoO_2 and MoO_3 nanowire arrays are 6.24 MV/m, 5.60 MV/m and 7.65 MV/m, respectively. Nanowires of Mo oxides have better field emission performance than the metallic Mo nanowires. Therefore, it is not necessary to concern about the oxidation of the nanowires.

The emission characteristics were analyzed using the Fowler-Nordheim (F-N) theory: $J \propto (E^2\beta^2/\Phi) \times \exp(-B\Phi^{1.5}/E\beta)$, where J is the emission current density, E is the applied field ($E = V/d$), Φ is the work function, β is the enhanced factor, and $B = 6.83 \times 10^9$ ($\mathrm{VeV^{-3/2}Vm^{-1}}$).[125] By plotting $\ln(J/E^2)$ versus $1/E$, a straight line can be obtained (insertion in Fig. 20). The linearity of these curves implies that the field emission from these nanowire arrays following the F-N theory. By using the work function of bulk Mo (4.24 eV), the β of our Mo nanowire arrays was calculated to be about 4400, which is high enough for various applications of field emission.

5.2.2. *Work Function at the Tip of a Nanowire/Nanobelt*

The workfunctions published in the literature are for bulk surfaces that do not have a curvature. For nanowire based materials, such as ZnO,[126] it is the workfunction at the tip of the nanowire that matters to the field emission. In this section, we demonstrate a technique for measuring the workfunction at the tip of a single nanotube/nanowire.[127, 128] The measurement was done by *in-situ* TEM. Figure 21(a) shows is a low magnification TEM image showing the experimental technique for the measurement of the workfunction at the tip of a ZnO nanobelt. One end of a nanobelt was electrically attached to a gold wire, and the other end faces directly against a gold ball. Because of the difference in the surface work function between the ZnO nanobelt and the counter Au ball, a static charge Q_0 exists at the tip of the nanobelt to balance this potential difference. The magnitude of Q_0 is proportional to the difference between work function of the nanobelt tip (NBT) and the Au electrode, $Q_0 = \alpha(\phi_{Au} - \phi_{NBT})$, where α is related to the geometry and distance between the nanobelt and the electrode.

The measurement is based on the mechanical resonance of the nanobelt induced by an externally alternative electric field. ZnO nanobelt can be regarded as a vibration cantilever clamped at one end. Experimentally, a constant voltage V_{dc} and an oscillating voltage $V_{ac}\cos 2\pi ft$ are applied onto the nanobelt (Fig. 21(a)), where f is the frequency and V_{ac} is the amplitude. Thus, the total induced charge on the nanobelt is

$$Q = Q_0 + \alpha e(V_{dc} + V_{ac}\cos 2\pi ft) \quad (15)$$

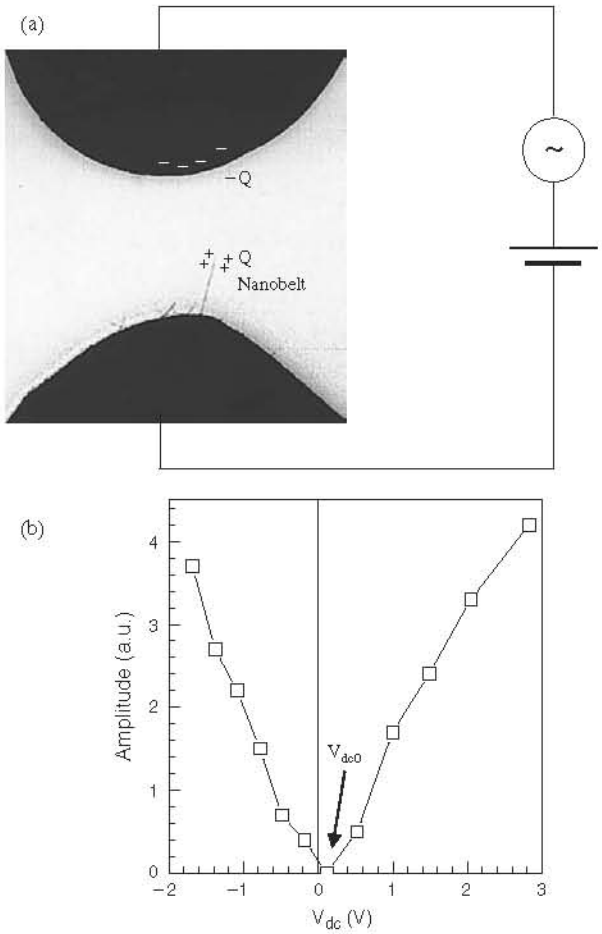

Fig. 21. (a) Experimental set up for measuring the work function at the tip of a ZnO nanobelt (see text). (b) A plot of vibration amplitude of a ZnO nanobelt as a function of the applied direct current voltage, from which, the offset voltage $V_{dc0} = 0.12$ V.

The force acting on the nanobelt is proportional to the square of the total charge on the nanobelt

$$\begin{aligned} F &= \beta[Q_0 + \alpha e(V_{dc} + V_{ac}\cos 2\pi ft)]^2 \\ &= \alpha^2\beta\{[(\phi_{Au} - \phi_{NBT} + eV_{dc})^2 + e^2V_{ac}^2/2] \\ &\quad + 2eV_{ac}(\phi_{Au} - \phi_{NBT} + eV_{dc})\cos 2\pi ft \\ &\quad + e^2V_{ac}^2/2\cos 4\pi ft\} \end{aligned} \quad (16)$$

where β is a proportional constant. In Eq. (15), the first term is constant and it causes a static deflection of the ZnO nanobelt. The second term is a linear term, and the resonance occurs if the applied frequency f is tuned to the intrinsic mechanical resonance frequency f_0 of the ZnO nanobelt. According to vibration theory and with consideration the rectangular cross-section of the nanobelt, mechanical resonance could be along the thickness or width direction. The last term in Eq. (16) is the second harmonics. The most important result of Eq. (16) is that, for the linear term, the resonance amplitude A of the nanobelt is proportional to $V_{ac}(\phi_{Au} - \phi_{NBT} + eV_{dc})$.

The principle of the measurement is as follows. We first set $V_{dc} = 0$ and tune the frequency f to get the mechanical resonance induced by the applied oscillating field. Second, under the resonance condition of keeping $f = f_0$ and V_{ac} constant, slowly change the magnitude of V_{dc} from zero to a value V_{dc0} that satisfies $\phi_{Au} - \phi_{NBT} + eV_{dc0} = 0$. At this moment, the resonance amplitude A becomes zero although the external AC voltage is still in effect. Therefore, the work function at the tip of ZnO nanobelt is $\phi_{NBT} = \phi_{Au} + eV_{dc0}$, while $\phi_{Au} = 5.1$ eV.[21] Figure 21(b) is a plot of the vibration amplitude A of the nanobelt as a function of the applied direct current voltage V_{dc}, from which the value for V_{dc0} is determined. The dual-mode resonance of the nanobelts have been observed experimentally.[22] It is important to point out that it does not matter which resonance direction/frequency one chooses, either along the thickness or width direction, the measured V_{dc0} remains the same.

To investigate the dependence of the work function of ZnO nanobelts on the size of their cross-section, i.e., the width W and thickness T of the nanobelts, we measured the geometrical size of the nanobelts from which the work function was measured. Using the projected dimension measured from the TEM image and the orientated angle determined from the corresponding electron diffraction pattern, the geometrical parameters of the nanobelts are obtained.[22] The work function at the tip of the ZnO nanobelt is around 5.2 eV, and shows no significant dependence on the cross-section size of the ZnO nanobelts. The technique demonstrated here can be applied to any type of nanowires/nanotubes.

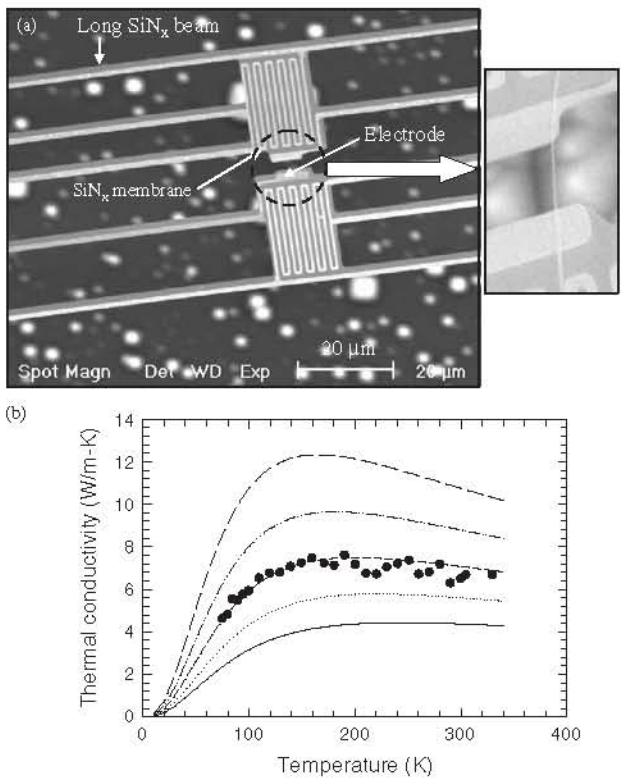

Fig. 22. (a) A microfabricated device for measuring the thermal conductivity of nanotubes, nanowires, and nanobelts. (b) Thermal conductivity of a 53 nm thick SnO_2 nanobelt as a function of temperature. Circles: measurement results; Lines: calculation results using the full dispersions transmission function approach with $FL = 10.5$ nm, 14.8 nm, 21 nm, 29.7 nm, and 42 nm, respectively for the five curves in the order of increasing thermal conductivity, where L is the characteristic length of the system, F is a parameter representing specularity of phonon reflection at the boundaries.

5.3. Heat Transfer Through a Nanobelt

Heat transfer at nanoscale is a very interesting and technologically important area. With the decrease of object size, phonon modes and phonon density of states change drastically, resulting in unusual thermal transport phenomena in mesoscopic systems. Theoretical investigation of thermal conductance in a one dimensional nanowire predicted quantum effect at very low temperature: $G_{th} = \pi^2 k_B^2 T/3h$.[129] Experimental measurement has proved the prediction.[130] Thermal transport along a single SnO_2 nanobelt has also been carried out (Fig. 22(a)).[131] Thermal contact micro-pads have been fabricated using lithography technique. The thermal conductance across the nanobelt was measured as a function of the local temperature is given in Figure 22(b). The thermal conductivity of the nanobelts is significantly suppressed in comparison to bulk due to increased phonon-boundary scattering and modified phonon dispersion.[132] This size effect can lead to localized heating in nanoelectronics,[133] but may find potential use for improving thermoelectric performance.

5.4. Gas Sensors

Conductometric metal oxide semiconductor thin films are the most promising devices among solid state chemical sensors, due to their small dimension, low cost, low power consumption, on-line operation and high compatibility with microelectronic processing. The fundamental sensing mechanism of metal oxide based gas sensors relies on a change in electrical conductivity due to the interaction process between the surface complexes such as O^-, O_2^-, H^+ and OH^- reactive chemical species and the gas molecules to be detected.

Although a large number of different oxides have been investigated for their gas sensing properties, commercially available gas sensors are mainly made of SnO_2 in the form of thick films, porous pellets or thin films. The effects of the microstructure, namely, ratio of surface area to volume, grain size and pore size of the metal oxide particles, as well as film thickness of the sensor are well recognized. Lack of long term stability has until today prevented a wide range application of this type of sensors. Nanobelts of semiconducting oxide, with a rectangular cross section in a ribbon-like morphology, are very promising for sensors due to the fact that the surface to volume ratio is very high, the oxide is single crystalline, the faces exposed

to the gaseous environment are always the same and the size is likely to produce a complete depletion of carriers inside the belt.[134] Beside the deposition technique is very simple and cheap, the size and shape can be easily controlled. In the polycrystalline and thick film devices, only a small fraction of the adsorbed species adsorbed near the grain boundaries is active in modifying the device electrical transport properties. In the new sensors based on single crystalline nanobelts, almost all of the adsorbed species are active in producing a surface depletion layer. Free carriers should cross the belts bulk along the axis in a FET channel-like way. Beside, since the size of the depletion layer for tin oxide, due to oxygen desorption, penetrates 50 nm or more through the bulk, the belts are probably almost depleted of carriers as a pinched-off FET because of belt thickness is typically less than 50 nm. The presence of poisoning species should switch the structures from pinched-off to conductive channel, strongly modifying the electrical properties. A further reduction of belt size could envisage the development of quantum confined structures and nanodevices.

For the fabrication of sensors, a platinum interdigitative electrode structure was made using lithography and metal deposition technique on an alumina substrate. A platinum heater was attached to the backside of the substrate in order to control the working temperature of the sensor. Then, a bunch of nanobelts was placed onto the electrodes for measuring their electric conductance, and a proper measure was taken to ensure the contact of the nanobelts with the electrodes. The flow-through technique is used to determine the gas-sensing properties of the thin films. A constant flux of synthetic air equal to 0.3 l/min, mixed with the desired amount of gaseous species, flows through a stabilized sealed chamber at 20 °C, atmospheric pressure and controlled humidity. Electrical characterization was carried out by a volt-amperometric technique at constant bias of 1 V, and a picoammeter measured the change of electrical current.

Figure 23(b) reports the isothermal response of the current flowing through the tin oxide nanobelt (Fig. 23(a)) when it was exposed to NO_2 gas of various concentrations. Figure 23(c) is the sensor response to the exposure of ppb level of dimethyl methyl phosphonate (DMMP), a nerve agent stimulant, show superior sensitivity to the gas.[135]

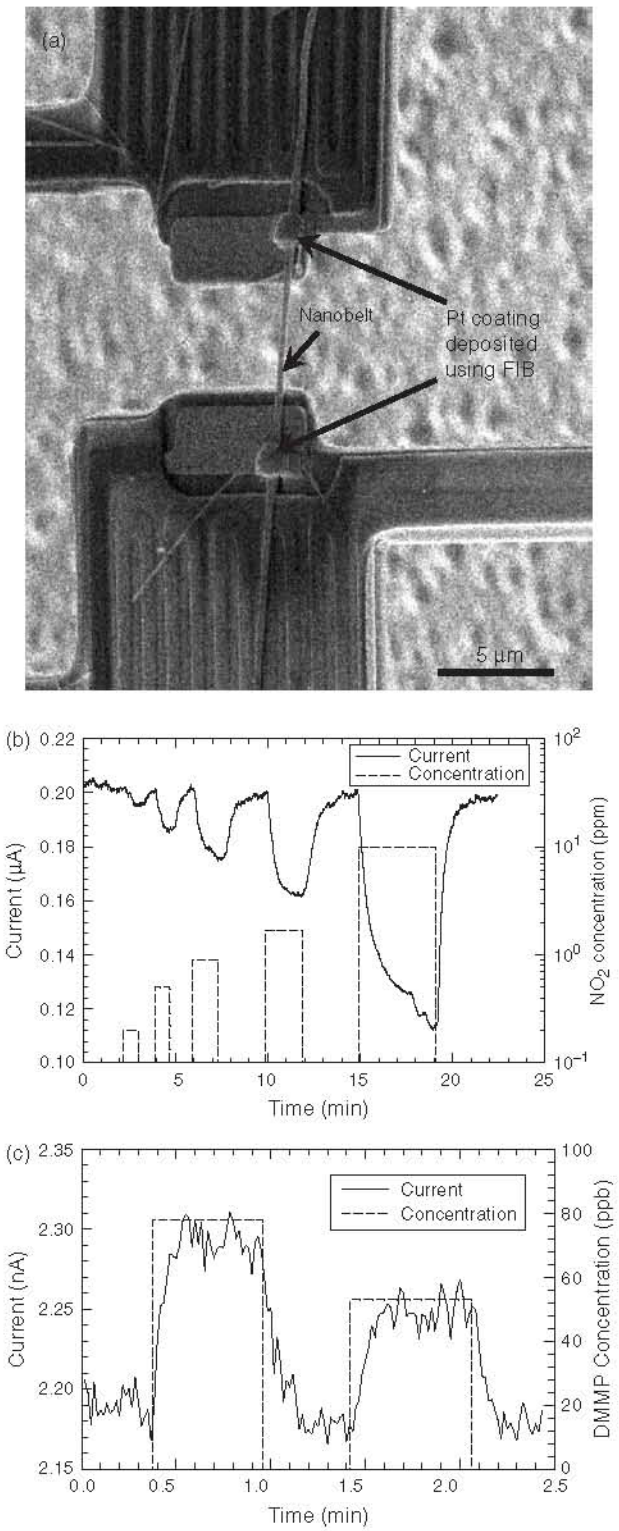

Fig. 23. Field effect transistor based gas sensors made using single nanobelt, and its application for detecting NO_2 DMMP.

5.5. Stability of Nanobelt FET

The as-grown ZnO nanostructure is naturally *n*-type semiconductor and its electronic property strongly relies on the oxygen deficiency and distribution in the structures. Therefore, investigation of oxygen diffusion was performed on a ZnO nanobelt device.[34] For this purpose, a ZnO nanobelt was placed between two Au electrodes and subsequently coated by a 50-nm Si_3N_4 layer to isolate ZnO nanobelt from contacting the atmosphere. Half of the deposited Si_3N_4 was then milled off by focus ion beam (FIB) for oxygen absorption, as shown schematically in Figure 24(a). The current–voltage characteristic of the ZnO nanobelt device (inset of Fig. 24(b)) is then measured

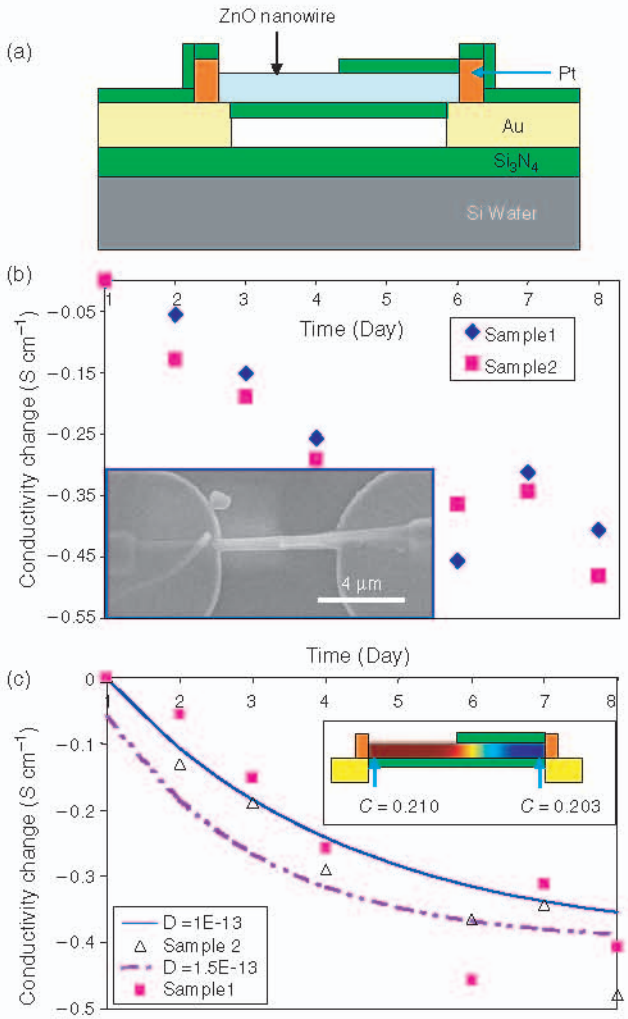

Fig. 24. (a) Schematic of ZnO nanowire placed on pre-patterned Au electrodes after Si_3N_4 deposition. (b) Conductivity change of ZnO nanowires over time. The inset shows the SEM image of the device. (c) Illustration of curve fitting to determine the oxygen diffusion coefficient. The continuous lines represent the simulated results while the dots represent the experimental results. The inset shows simulated oxygen distribution on the eighth day after ion milling process.

on a daily basis throughout one week. The measured conductivity change on two such samples as a function of time is shown in Figure 24(b). It was found that the conductivity almost dropped linearly with the increasing of days when the ZnO nanobelt was exposed in air.

In order to explain the behavior of the observed conductivity change, a simulation of the oxygen diffusion was constructed by assuming:

(1) a uniform distribution of defects along the nanobelt's volume;

(2) oxygen molecules adhered to the surface of ZnO broke down to single oxygen atoms, which remained the same molecular concentration as the oxygen molecule in atmosphere; and

(3) no oxygen diffused through the Si_3N_4 insulating layer.

The inset of Figure 24(c) illustrates the oxygen concentration distribution profile on the eighth day. Based on semiconductor theory, the conductivity in *n*-type ZnO can be given by:

$$\Delta\sigma(t) \approx -2e \cdot \mu^e \cdot \Delta C_0(t)$$

where $\Delta\sigma(t)$ is the conductivity change of ZnO as a function of time, e is the charge of an electron, μ_e is the electron mobility in ZnO and $\Delta C_o(t)$ is the concentration change of oxygen vacancies due to diffusion. $\Delta C_o(t)$ could be obtained from simulation, and μ_e is known for ZnO nanowire/nanobelt through a previous measurement to be around 17 cm^2/V · s.[35] So it is possible to plot a curve of conductivity versus time change as shown in Figure 24(c). By comprising the experimentally measured conductivity and that simulated using finite element analysis (FEA), we were able to derive the diffusion coefficient of oxygen in ZnO nanowires/nanobelts.

5.6. Optical Property

Optical properties of NWs and NBs are important for many of their technological applications. We have recently grown ultrasmall nanobelts with the VLS growth using a novel catalyst.[136] Instead of using dispersive nanoparticles as the catalyst for seeded growth, a uniform thin film (~10 nm) of tin was coated on the silicon substrate. The ZnO nanobelts produced by the tin film catalyst are rather narrow, thin and uniform (Fig. 25(a)). Electron diffraction pattern and high-resolution TEM image show that the nanobelts grow along [0001], its top surfaces are $(2\bar{1}\bar{1}0)$ and the side surfaces are $(0\bar{1}10)$. The average diameter of the nanobelts is 5.5 nm with a standard deviation of ±1.5 nm, indicating a very good size uniformity.

To examine the size induced quantum effect of the ultra thin ZnO nanobelts, photoluminescence (PL) measurements were performed at room temperature using a Xe lamp with an excitation wavelength of 330 nm (Fig. 25(b)). In comparison to the PL from nanobelts of an average width of ~200 nm, the 6 nm nanobelts have a 14 nm shift in the emission peak, which possibly indicate quantum confinement due to the reduced size of the nanobelts.

5.7. Crossed Nanowire pn Junction

p-n photodiode is an alternative form of photoconductor and can be constructed with crossed nanowires.[137, 138] By combining with wide bandgap materials, such as ZnO, SnO_2, and ZnS, the whole range of light from ultraviolet to the near infrared can be effectively absorbed by this kind of photodiode. We report the performance of a prototype nanoscale photodiode based on the crossed structure of a *p*-type Zn_3P_2 NW with an *n*-type ZnO NW.[139] In order to form the required nano heterojunction, we aligned a Zn_3P_2 NW between two Au electrodes and fixed it with Pt metal via a FIB, which can improve the contact. After

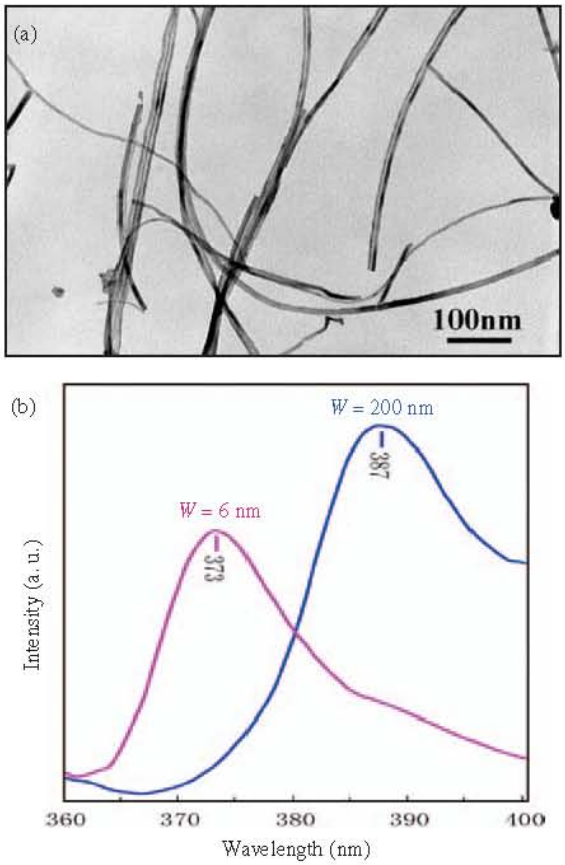

Fig. 25. (a) Low magnification TEM image showing the size uniformity of ZnO nanobelts. (b) Photoluminescence spectra acquired from the $W = 200$ nm-wide ZnO nanobelts and the $W = 6$ nm-wide ZnO nanobelts.

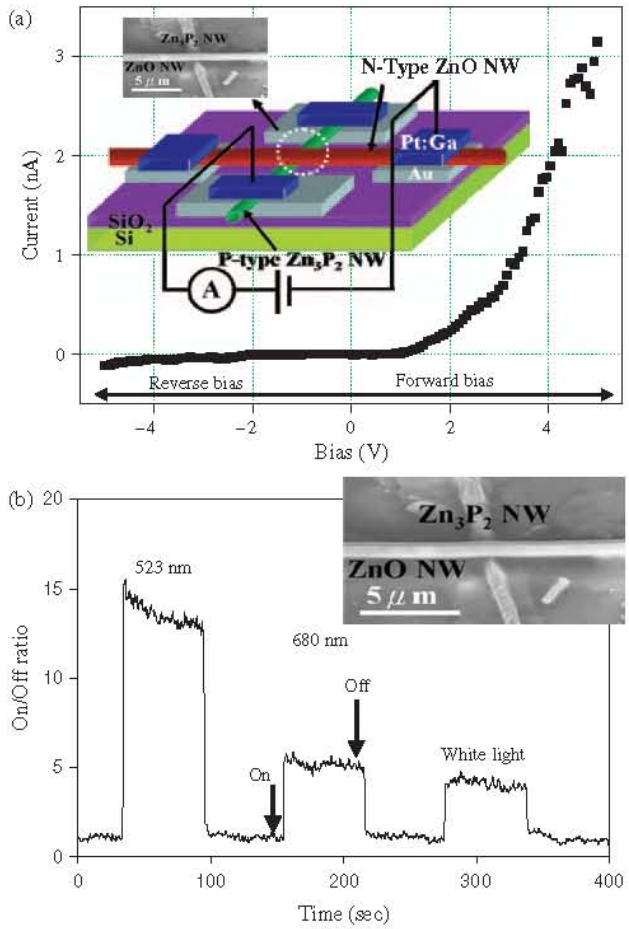

Fig. 26. (a) I–V curve for ZnO/Zn_3P_2 nanoscale heterojunction at reverse and forward bias. Inset shows the prototype of the nanodevice, in which a ZnO NW was placed on top of a Zn_3P_2 NW. (b) The on/off ratio as a function of the time under red (680 nm), green (523 nm), or white light illumination, respectively. The inset is the schematic of the device.

that, a ZnO NW was aligned perpendicular to Zn_3P_2 NW by diaphoresis technique and connected to another pair of Au electrodes via Pt deposition by FIB microscopy. The final structure and schematic diagram are illustrated in insets of Figure 26(a). The composition of the two NWs is confirmed with EDS and an ohmic contact is achieved individually for both ZnO and Zn_3P_2.

The photon response of the photodiode to different lights is shown in Figure 26(b) in which we applied a fixed reverse bias of 5 V and turned on and off green light (523 nm), red light (680 nm), and the white light lamp serially. Green light produces the highest (~13) on/off ratio as expected. Interestingly, the dim white light also produces an on/off ratio (~5) which is significantly greater than one, indicating the high sensitivity of the photodiode to visible lights. Furthermore, the response time for all tested lights is below one second. The very nice performance of the diode may result from the following advantages. First of all, the top ZnO NW has a wide band gap and the light from infrared to violet can penetrate easily with minimum energy loss. Second, the depletion region is mostly located at Zn_3P_2 NW side so that electron-hole pairs can be generated by a wide light range from 380–800 nm, and significant generation current enhancement results. Finally, the large minority diffusion length of Zn_3P_2 enables more photon generated minority carriers in the neutral region to diffuse into the depletion region and results in a large on/off ratio and high sensitivity as well. The high sensitivity, quick response and nanoscale size can benefit the ZnO/Zn_3P_2 nanoscale heterojunction as a candidate for a high efficient and spatial resolved photon.

5.8. Piezoelectric Properties

Piezoelectricity is due to the atomic scale polarization. To illustrate the piezoelectricity, one considers an atom with a positive charge that is surrounded tetrahedrally by anions (Fig. 27(a)). The center of gravity of the negative charges is at the center of the tetrahedron. By exerting a pressure on the crystal along the cornering direction of the tetrahedron, the tetrahedron will experience a distortion and the center of gravity of the negative charges will no longer coincide with the position of the positive central atom, an

RESEARCH ARTICLE

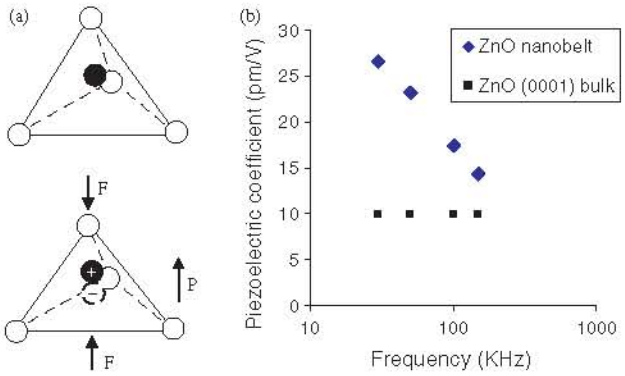

Fig. 27. (a) Schematics showing piezoelectric effect in tetrahedrally coordinated cation-anion unit. (b) Experimentally measured piezoelectric coefficient d_{33} for ZnO and its comparison to that of the bulk (The experiments were carried out by Prof. Scott Mao and Minhua Zhao, University of Pittsburgh). ~~Figure 11. (a) Experimental set up and procedures for generating electricity by deforming a piezoelectric NW using a conductive AFM tip. (b) Output voltage image map of ZnO NW arrays.~~

electric dipole is generated. If all of the tetrahedra in the crystal have the same orientation or some other mutual orientation that does not allow for a cancellation among the dipoles, the crystal will have a macroscopic dipole. The two opposite faces of the crystal have opposite electric charges.

The piezoelectricity refers to a reverse process in which a contraction or elongation is created to the crystal once it is positioned in an electric field. Crystals can only be piezoelectric if they are non-central symmetric to ensure the non-compensation among the dipoles created by the tetrahedra. Piezoelectric effect can convert a mechanical vibration into an electric signal or vice versa. It is widely used in resonators, controlling tip movement in scanning probe microscopy, sensors for vibration waves in air and under sea etc.

Piezoelectricity is an intrinsic property of ZnO, and the piezoelectricity is not induced by the polar surfaces. The magnitude of the piezoelectric effect depends on the growth direction of the nanobelt. The piezoelectric coefficient of ZnO nanobelt has been measured by atomic force microscopy using a conductive tip.[140] After coating (100) Si wafer with a 100 nm Pd, ZnO nanobelts were dispersed on the conductive surface. Then the whole surface was coated with another 5 nm Pd coating, which served as an electrode on ZnO nanobelt to get uniform electric field and avoid electrostatic effect. Extra care was taken to ensure that top and bottom surface of the nanobelt was not short circuited after Pd deposition. The ZnO nanobelt was located by a commercially available AFM under tapping mode. Piezoresponse force microscopy (PFM) is used to measure the effective piezoelectric coefficient (d_{33}) of individual (0001) surface dominated zinc oxide nanobelt lying on conductive surface. Based on references of bulk (0001) ZnO and x-cut quartz, effective piezoelectric coefficient d_{33} of ZnO nanobelt is found to be frequency dependent and varies from 14.3 pm/V to 26.7 pm/V (Fig. 27(b)), which is much larger than that of the bulk (0001) ZnO of 9.93 pm/V. The results project the applications of ZnO nanobelts as nanosensors and nanoactuators.

5.9. Nanogenerators and Nano-Piezotronics

ZnO is a unique material that simultaneously exhibits semiconducting and piezoelectric properties. The coupling of these two properties can realize some unique functions that can never been achieved by other materials. In this section, we will introduce nanogenerators based on aligned ZnO NWs exploring those novel functions.

Using piezoelectric ZnO NW arrays, we have discovered an innovative phenomenon on converting nano-scale mechanical energy into electric energy.[141, 142] The measurements were performed by AFM using a Si tip coated with Pt. In the AFM contact mode, a constant normal force of 5 nN was maintained between the tip and sample surface. The tip scanned over the top of the ZnO NWs, which were thus bent and then released. The output voltage across an outside load of resistance $R_L = 500$ MΩ was continuously monitored while the tip scanned over the nanowires, as shown in Figure 28(a). Meanwhile, the corresponding output voltages across the load were recorded. In the output voltage image shown in Figure 28(b), many sharp output voltage peaks (like discharge peaks) have been observed,

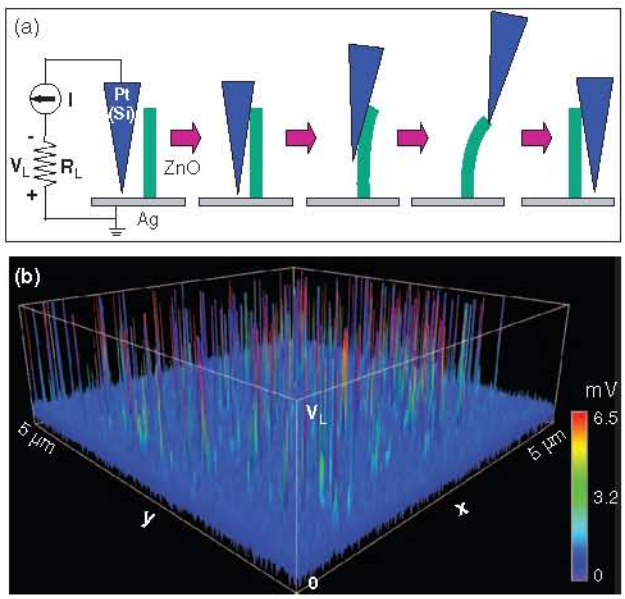

Fig. 28. (a) Experimental set up and procedures for generating electricity by deforming a piezoelectric NW using a conductive AFM tip. The root of the NW is grounded, and an external load of $R_L = 500$ MΩ is applied, which is much larger than the inner resistance R_I of the NW. The AFM scans across the NW arrays in contact mode. (b) Output voltage image of the NW arrays when the AFM tip scans across the NW arrays. The discharging process is so quick that each discharge event is characterized by only a couple of data points. This gives a difficulty of displaying the data by rainbow color.

RESEARCH ARTICLE

which are typically about 4–50 times higher than the noise level and Most of the voltage peaks were ~6–9 mV in height. The density of NWs contacted by the tip was counted to be ~20/μm^2, and the average density of NWs whose voltage output events had been captured by the tip is ~8/μm^2, thus ~40% of the NWs were contacted.

The physical principle for creating the piezoelectric discharge energy is related to the uniquely coupled piezoelectric and semiconducting dual properties of ZnO. For a vertical straight ZnO NW (Fig. 29(a)), the deflection of the NW by AFM tip creates a strain field, with the outer surface (right-hand side) being stretched (positive strain ε) and inner surface (right-hand side) compressed (negative strain ε) (Fig. 29(b)). Due to the electric-mechanical coupling characteristic of ZnO, electric field E_z along the NW (z direction) will be created inside its volume due to piezoelectric effect, $E_z = \varepsilon_z/d$, where d_{33} is the piezoelectric

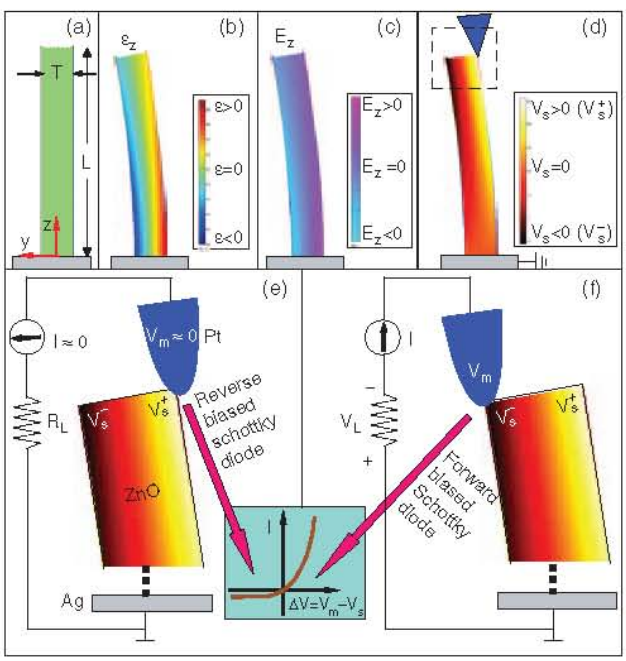

Fig. 29. Physical principle of the observed power generation process of a piezoelectric ZnO NW, showing a unique coupling of piezoelectric and semiconducting properties in this metal-semiconductor Schottky barrier governed transport process. (a) Schematic definition of a NW and the coordination system. (b) Longitudinal strain ε_z distribution in the NW after being deflected by an AFM tip from the side. The data was simulated by FEMLAB for a ZnO NW of length 1 μm, aspect ration of 10. (c) The corresponding longitudinal piezoelectric induced electric field E_z distribution in the NW. (d) Potential distribution in the NW as a result of piezoelectric effect. The dashed box indicates the area to be examined in details in (e, f). (e, f) Metal and semiconductor contacts between the AFM tip and the semiconductor ZnO NW at two reversed local contact potentials (positive and negative), showing reverse and forward biased Schottky rectifying behavior, respectively (see text). It is this oppositely biased Schottky barrier across the NW makes it possible to preserve the piezoelectric charges and later produce the discharge output. Inset is a typical I–V characteristic of a metal-semiconductor (n-type) Schottky barrier. The process in (e) is built up the potential; the process in (f) is to discharge the potential.

coefficient along the nanowire direction that is normally the positive c-axis with Zn atomic layer being the front terminating layer.[38] The piezo-electric field direction is closely parallel to the z-axis (NW direction) at the outer surface and anti-parallel to the z-axis at the inner surface (Fig. 29(c)). Under the first order approximation, across the width of the NW at the top end, the electric potential distribution from the left-hand side surface (compressed) to the right-hand side surface (stretched) is approximately between V_s^- to V_s^+ ~~($V_s^{\mp} = \mp 3Ty_m/4Ld$, where T is the thickness of the NW)~~. The electrode at the root of the NW is grounded. The potential is created by the relative displacement of the Zn^{2+} cations with respect to the O^{2-} anions due to piezoelectric effect in the wurtzite crystal structure; thus, these ionic charges cannot freely move and cannot recombine without releasing the strain (Fig. 29(d)). The potential difference is maintained as long as the deformation is in place and no foreign free charges (such as from the metal contacts) are injected.

In experimental design, the contacts at the top and the root of the NW were non-symmetric. The contact at the bottom was between ZnO and silver paste, which was Ohmic. At the tip of the NW, however, the contact between Pt and ZnO was Schottky, which dominates the entire transport process. In the first step, the AFM conductive tip that induces the deformation is in contact with the stretched surface of positive potential V_s^+ (Figs. 29(d and e)). Since the Pt metal tip has a potential of nearly zero, $V_m = 0$, the metal tip-ZnO interface is negatively biased for $\Delta V = V_m - V_s^+ < 0$. With consideration the n-type semiconductor characteristic of the as-synthesized ZnO NWs, the Pt metal-ZnO semiconductor (M-S) interface in this case is a reversely biased Schottky diode (Fig. 29(e)), resulting in little current flowing across the interface. In the second step, when the AFM tip is in contact with the compressed side of the NW (Fig. 29(f)), the metal-ZnO interface is positively biased for $\Delta V = V_L = V_m - V_s^- > 0$. The M-S interface in this case is a positively biased Schottky diode, resulting in a sudden increase in the output electric current, e.g., a sharp increase in output voltage V_L (positive). The current is the result of ΔV driven flow of electrons from the semiconductor ZnO NW to the metal tip. The flow of the free electrons from the loop through the NW to the tip will neutralize the ionic charges distributed in the volume of the NW and thus reduce the magnitude of the potential V_s^- and V_s^+. Therefore, the output voltage V_L starts to drop and reaches zero until all of the ionic charges in the NW are fully neutralized. It is also important to note that the discharge occurs when the NW is bent nearly to the maximum deflection according to the model, which is in agreement with the observation. The principle demonstrated here is the fundamental mechanism of nano-piezotronics, a new field of utilizing piezoelectric effect for fabricating unique and novel electromechanically coupled electronic devices and components.

RESEARCH ARTICLE

6. BIOCOMPATIBILITY AND BIODEGRADABILITY

In parallel of exploring the exciting physical and chemical properties of NWs and NBs, it is also required to study their bio-safety, biocompatible and bio-degradability. But very limited literatures are available. Recently, we present the first study on bio-degradability and biocompatibility of ZnO wires/belts.[143] A systematic study about the etching and dissolving behavior ZnO wires in various solutions with moderate pH values, including deionized water, ammonia, NaOH solution, and horse blood serum. The result shows that ZnO can be dissolved by deionized water (pH ~ 4.5–5.0), ammonia (pH ~ 6.8–7.1, 8.7–9.0) and NaOH solution (pH ~ 6.8–7.1, 8.7–9.0). The study of interaction of ZnO wires with horse blood serum shows that the ZnO wires can survive in the fluid for a few hours, and then they will degrade in the horse blood serum into mineral ions.

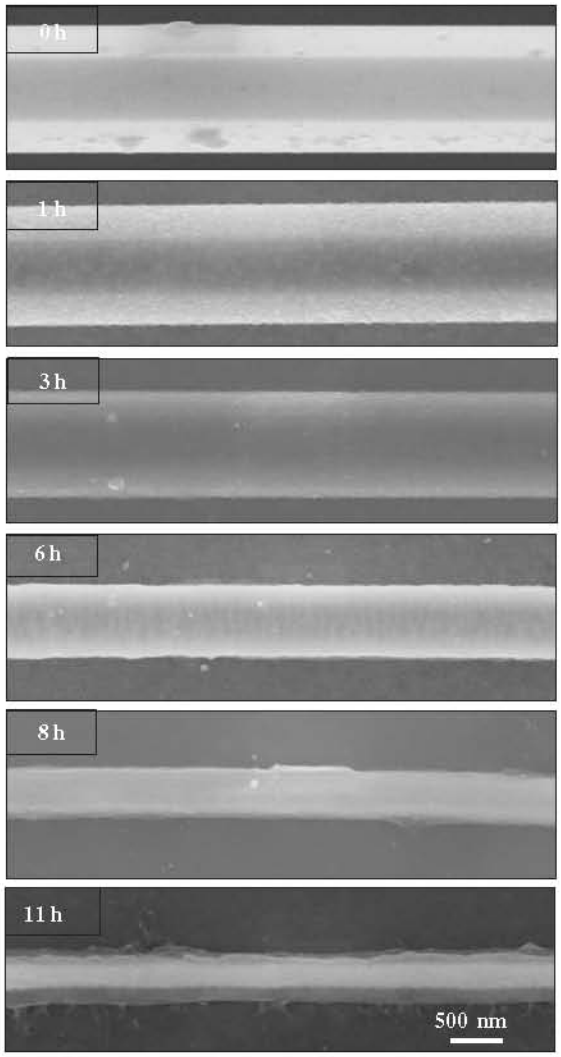

Fig. 30. SEM images of a ZnO wire that has interacted with horse blood serum solution (10% concentration, pH ~ 7.9–8.2) for different lengths of time.

Figure 30 shows SEM images of an ZnO wire that had been dipped into diluted horse blood serum (10% concentration, pH ~ 7.9–8.2) with NaOH for 0, 1, 3, 6, 8 and 11 hours, respectively. After 1 hour in the solution, there is no visible etching on the wire surface except some adsorbed species (Fig. 5(b)). The etching became severe after 3 hour of interaction, as indicated by the reduced wire diameter. After etching for 11 hours, ~94% volume of the ZnO wire was dissolved. We estimated that no more than 12 hours, the ZnO wire would be totally etched by the horse blood serum.

The implication of this study is enormous. First, ZnO has the potential to be used for biosensors, and it requires a reasonable time to function in biological systems to perform device function. Secondly, if the ZnO wire is lost in the body or in blood vessel, it can eventually dissolve into ions in the solution, which can be adequately adsorbed by the body and become part of the nutrition. The biodegradability and biocompatibility of ZnO wires make it suitable for *in-situ* biosensing and biodetection.

7. OUTLOOK

In this review, we have illustrated and addressed the key issues regarding the synthesis, structure characterization and properties of oxide NWs and NBs. The NWs and NBs as well as their hierarchical nanostructures have unique and important applications in nano-size optical, sensor and optoelectronic devices. As for the future nanotechnology and applications in nanosystems and biotechnology, there are a few key issues that we have to investigate related to NW and NB growth:

(1) Fundamental understanding about the growth mechanisms. The VLS growth process has been successfully developed and its growth process is reasonably well understood. Fundamental understanding on the surface physical chemical process and the process at catalyst-nanostructure interface are essential for optimizing and controlling growth. Although we have shown some success in NW and NB growth using the VS process, but the understanding of the growth mechanism is relatively poor.

(2) Fundamental understanding on growth kinetics. We have elaborated the key role played by growth kinetics in the growth of 1D nanostructures. Growth of 1D nanostructure is a thermodynamically non-equilibrium process and it is controlled by kinetics, but growth kinetics is a rather complex process. A solid understanding on growth kinetics is essential for controlling the growth process.

(3) Structurally, morphologically and dimensionally controlled synthesis. For large-scale integration we need NWs and NBs that have uniform dimensionality and well-defined morphology. Controlling the surface structure of NWs and NBs would have equivalent importance as controlling the helical angle of carbon nanotubes, which determines the semiconductor or metallic behavior of the

nanotube. Property control is possible only if structural control is achieved. Techniques are required to grow the designed structure with superior controllability in size, size distribution, shape, crystal structure, defect distribution, and even surface structure. Experimental methods are also needed for separating NWs or NBs exhibiting different structure characteristics.

(4) Large-scale patterned and designed/targeted growth as well as self-organization. Future applications and nanomanufacturing will strongly rely on designed growth and self-assembly technology. We would like to control the location of NW growth, the number, location and orientation of NWs to be grown. This is an essential step in integrating nanostructures with existing technologies.

(5) Growth of hierarchical and multifunctional NWs and NBs. The growth of NWs can be controlled axially and longitudinally. Growth of composite NWs and NBs with multifunctionality will be important for novel devices.

(6) Self-assembly of functionalized nanowires and nanobelts with distinct selectivity. For the fabrication of an array of devices that have specific individual functions, techniques are required to self-assemble the NWs/NBs into a predesigned pattern for massive fabrication of devices. The self-assembly should be as less steps as possible.

(7) Interfacing with biosystems. Biosystem is the most complex system that we can ever imagine of. We first need to examine the stability, sensitivity and the effectiveness of nanodevices in biofluid. Then the interfacing and interaction of NWs and NBs with biological species, such as cells, remain studied. Finally, bio-safety must be examined to avoid serious side-effects.

The literature in NW and NB related areas is huge and every year now has over 1000 papers being published, and the number of publications increase exponentially. There are many progresses being made in the area. This review only covers a fraction of the progress in the field.

Acknowledgments: Thanks to Y. Ding, P. X. Gao, J. H. Song, X. D. Wang, R. S. Yang, C. S. Lao, L. Shi, W. L. Hughes, B. Buchine, W. J. Mai, X. Y. Kong, J. Liu, C. Ma, X. D. Bai, H. Liu, C. G. Hu, Y. L. Chueh, J. Zhou, C. J. Summers, S. X. Mao, M. H. Zhao, N. S. Xu, L. J. Chou, J. H. He, L. J. Chen, and Z. W. Pan for their contributions to the work reviewed in this article. We acknowledge generous support from DARPA, NSF, NASA and NIH.

References and Notes

1. Z. L. Wang (ed.), Nanowires and Nanobelts—materials, properties and devices, Vol. I: Metal and Semiconductor Nanowires, Vol: II, Nanowires and Nanobelts of Functional Materials, Kluwer Academic Publisher, Boston **(2003)**.
2. T. W. Odom, J. L. Huang, P. Kim, and C. M. Lieber, *Nature* 391, 62 **(1998)**.
3. T. Odom, J. Huang, P. Kim, and C. M. Lieber, *J. Phys. Chem. B* 104, 2794 **(2000)**.
4. C. Dekker, *Phys. Today* 52, 22 **(1999)**.
5. H. Dai, J. Kong, C. Zhou, N. Franklin, T. Tmobler, A. Cassell, S. Fan, and M. Chapline, *J. Phys. Chem. B* 103, 11246 **(1999)**.
6. S. J. Tanš, R. M. Verschueren, and C. Dekker, *Nature* 393, 49 **(1998)**.
7. R. Martel, T. Schmidt, H. R. Shea, T. Hertel, and P. Avouris, *Appl. Phys. Lett.* 73, 2447 **(1998)**.
8. Z. Yao, H. W. C. Postma, L. Balents, and C. Dekker, *Nature* 402, 273 **(1999)**.
9. M. S. Fuhrer, J. Nygrad, L. Shih, M. Forero, Y. G. Yoon, M. S. C. Mazzoni, H. J. Choi, J. Ihm, S. G. Louie, A. Zettl, and P. L. McEuen, *Science* 288, 494 **(2000)**.
10. V. Derycke, R. Martel, J. Appenzeller, and P. Avouris, *Nano Lett.* 1, 453 **(2001)**.
11. A. Bachtold, P. Hadley, T. Nakanishi, and C. Dekker, *Science* 294, 1317 **(2001)**.
12. P. G. Collins, M. S. Arnold, and P. Avouris, *Science* 292, 706 **(2001)**.
13. C. M. Lieber, *Solid State Commun.* 107, 106 **(1998)**.
14. J. Hu, T. W. Odom, and C. M. Lieber, *Acc. Chem. Res.* 32, 435 **(1999)**.
15. X. Duan and C. M. Lieber, *Adv. Mater.* 12, 298 **(2001)**.
16. M. S. Gudiksen, J. Wang, and C. M. Lieber, *J. Phys. Chem. B* 105, 4062 **(2001)**.
17. Y. Cui, X. Duan, J. Hu, and C. M. Lieber, *J. Phys. Chem. B* 104, 5213 **(2000)**.
18. X. Duan, Y. Huang, Y. Cui, J. Wang, and C. M. Lieber, *Nature* 409, 66 **(2001)**.
19. Y. Cui and C. M. Lieber, *Science* 291, 851 **(2001)**.
20. Y. Huang, X. Duan, Y. Cui, L. Lauhon, K. Kim, and C. M. Lieber, *Science* 294, 1313 **(2001)**.
21. Z. W. Pan, Z. R. Dai, and Z. L. Wang, *Science* 209, 1947 **(2001)**.
22. Z. R. Dai, Z. W. Pan, and Z. L. Wang, *Adv. Funct. Mater.* 13, 9 **(2003)**.
23. X. Y. Kong and Z. L. Wang, *Nano Lett.* 3, 1625 **(2003)**.
24. Z. Y. Fan and J. G. Lu, *Appl. Phys. Lett.* 86, 032111 **(2005)**.
25. P. C. Chang, Z. Y. Fan, C. J. Chien, D. Stichtenoth, C. Ronning, and J. G. Lu, *Appl. Phys. Lett.* 89, 133113 **(2006)**.
26. Y. Huang, X. Duan, Q. Wei, and C. M. Lieber, *Science* 291, 630 **(2001)**.
27. F. Seker, K. Meeker, T. F. Kuech, and A. B. Ellis, *Chem. Rev.* 100, 2505 **(2000)**.
28. R. K. Iler, The Chemistry of Silica, Wiley, New York **(1979)**.
29. M. Arnold, P. Avouris, and Z. L. Wang, *Phys. Chem. B* 107, 659 **(2002)**.
30. E. Comini, G. Faglia, G. Sberveglieri, Z. W. Pan, and Z. L. Wang, *Appl. Phys. Lett.* 81, 1869 **(2002)**.
31. X. D. Bai, P. X. Gao, Z. L. Wang, and E. G. Wang, *Appl. Phys. Lett.* 82, 4806 **(2003)**.
32. W. Hughes and Z. L. Wang, *Appl. Phys. Lett.* 82, 2886 **(2003)**.
33. L. Shi, Q. Hao, C. Yu, D. Kim, N. Mingo, X. Y. Kong, and Z. L. Wang, *Appl. Phys. Lett.* 84, 2638 **(2004)**.
34. X. Y. Kong and Z. L. Wang, *Appl. Phys. Lett.* 84, 975 **(2004)**.
35. X. Y. Kong, Y. Ding, R. S. Yang, and Z. L. Wang, *Science* 303, 1348 **(2004)**.
36. J. G. Lu, P. C. Chang, and Z. Y. Fan, *Materials Science & Engineering R-Reports* 52, 49 **(2006)**.
37. R. S. Wagner and W. C. Ellis, *Appl. Phys. Lett.* 4, 89 **(1964)**.
38. R. S. Wagner, Whisker Technology, edited by A. P. Levitt, Wiley, New York **(1970)**.
39. T. J. Trentler, K. M. Hickman, S. C. Goel, A. M. Viano, P. C. Gibbons, and W. E. Buhro, *Science* 270, 1791 **(1995)**.
40. T. J. Trentler, S. C. Goel, K. M. Hickman, A. M. Viano, M. Y. Chiang, A. M. Beatty, P. C. Gibbons, and W. E. Buhro, *J. Am. Chem. Soc.* 119, 2172 **(1997)**.
41. P. Yang and C. M. Lieber, *Science* 273, 1836 **(1996)**.

42. P. Yang and C. M. Lieber, *J. Mater. Res.* 12, 2981 **(1997)**.
43. Z. R. Dai, Z. W. Pan, and Z. L. Wang, *J. Am. Chem. Soc.* 124, 8673 **(2002)**.
44. M. H. Huang, Y. Y. Wu, H. Feick, N. Tran, E. Weber, and P. D. Yang, *Adv. Mater.* 13, 113 **(2001)**.
45. M. S. Arnold, P. Avouris, Z. W. Pan, and Z. L. Wang, *J. Phys. Chem. B* 107, 659 **(2003)**.
46. E. Comini, G. Faglia, G. Sberveglieri, Z. W. Pan, and Z. L. Wang, *Appl. Phys. Lett.* 81, 1869 **(2003)**.
47. M. H. Huang, S. Mao, H. Feick, H. Yan, Y. Wu, H. Kind, E. Weber, R. Russo, and P. Yang, *Science* 292, 1897 **(2001)**.
48. C. Liu, J. A. Zapien, Y. Yao, X. Meng, C. S. Lee, S. Fan, Y. Lifshitz, and S. T. Lee, *Adv. Mater.* 15, 838 **(2003)**.
49. X. D. Bai, E. G. Wang, P. X. Gao, and Z. L. Wang, *Nano Lett.* 3, 1147 **(2003)**.
50. P. Yang, H. Q. Yan, S. Mao, R. Russo, J. Johnson, R. Saykally, N. Morris, J. Pham, R. R. He, and H. J. Choi, *Adv. Funct. Mater.* 12, 323 **(2002)**.
51. Q. X. Zhao, M. Willander, R. R. Morjan, Q. H. Hu, and E. E. B. Campbell, *Appl. Phys. Lett.* 83, 165 **(2003)**.
52. P. X. Gao, Y. Ding, and Z. L. Wang, *Nano Lett.* 3, 1315 **(2003)**.
53. W. I. Park, D. H. Kim, S. W. Jung, and G. C. Yi, *Appl. Phys. Lett.* 80, 4232 **(2002)**.
54. O. Harnack, C. Pacholski, H. Weller, A. Yasuda, and J. M. Wessels, *Nano Lett.* 3, 1097 **(2003)**.
55. B. Lei, C. Li, D. H. Zhang, S. Han, and C. W. Zhou, *J. Phys. Chem. B* 109, 18799 **(2005)**.
56. C. Li, B. Lei, Z. C. Luo, S. Han, Z. Q. Liu, D. H. Zhang, and C. W. Zhou, *Adv. Mater.* 17, 1548 **(2005)**.
57. K. Kempa, B. Kimball, J. Rybczynski, Z. P. Huang, P. F. Wu, D. Steeves, M. Sennett, M. Giersig, D. V. G. L. N. Rao, D. L. Carnahan, D. Z. Wang, J. Y. Lao, W. Z. Li, and Z. F. Ren, *Nano Lett.* 3, 13 **(2003)**.
58. Z. P. Huang, D. L. Carnahan, J. Rybczynski, M. Giersig, M. Senett, D. Z. Wang, J. G. Wen, K. Kempa, and Z. F. Ren, *Appl. Phys. Lett.* 82, 460 **(2003)**.
59. X. D. Wang, C. J. Summers, and Z. L. Wang, *Nano Lett.* 4, 423 **(2004)**.
60. P. X. Gao and Z. L. Wang, *J. Phys. Chem. B* 106, 12653 **(2002)**.
61. Z. W. Pan, Z. R. Dai, C. Ma, and Z. L. Wang, *J. Am. Chem. Soc.* 124, 1817 **(2002)**.
62. J. P. Schaffer, A. Saxena, S. D. Antolovich, T. H. Sanders, and S. B. Warner, Jr., The Science and Design of Engineering Materials, 2nd edn., McGraw-Hill, New York **(1999)**, Chap. 6.
63. X. D. Wang, C. J. Summers, and Z. L. Wang, *Adv. Mater.* 16, 1215 **(2004)**.
64. Z. L. Wang, Z. W. Pan, and Z. R. Dai, *Microsc. Microanal.* 8, 467 **(2002)**.
65. Z. R. Dai, Z. W. Pan, and Z. L. Wang, *J. Phys. Chem. B.* 106, 902 **(2002)**.
66. Z. W. Pan, Z. R. Dai, and Z. L. Wang, *Appl. Phys. Lett.* 80, 309 **(2001)**.
67. X. Y. Kòng, Y. Ding, and Z. L. Wang, *J. Phys. Chem. B* 108, 570 **(2004)**.
68. W. Hirschwald, *Z. Phys. Chem.* 77, 21 **(1972)**.
69. O. Dulub, L. A. Boatner, and U. Diebold, *Surf. Sci.* 519, 201 **(2002)**.
70. B. Meyer and D. Marx, *Phys. Rev. B* 67, 035403 **(2003)**.
71. P. W. Tasker, *J. Phys. C: Solid State Phys.* 12, 4977 **(1979)**.
72. O. Dulub, U. Diebold, and G. Kresse, *Phys. Rev. Lett.* 90, 016102 **(2003)**.
73. A. Wander, F. Schedin, P. Steadman, A. Norris, R. McGrath, T. S. Turner, G. Thornton, and N. M. Harrison, *Phys. Rev. Lett.* 86, 3811 **(2001)**.
74. V. Staemmler, K. Fink, B. Meyer, D. Marx, M. Kunat, S. Gil Girol, U. Burghaus, and Ch. Woll, *Phys. Rev. Lett.* 90, 106102 **(2003)**.
75. R. S. Yang, Y. Ding, and Z. L. Wang, *Nano Lett.* 4, 1309 **(2004)**.
76. X. Y. Kong and Z. L. Wang, *Appl. Phys. Lett.* 84, 975 **(2004)**.
77. Y. Ding, X. Y. Kong, and Z. L. Wang, *Phys. Rev. B* 70, 235408 **(2004)**.
78. V. Chandrasekhar, R. A. Webb, M. J. Brady, M. B. Ketchen, W. J. Gallagher, and M. J. Kleinsasser, *Phys. Rev. Lett.* 67, 3578 **(1991)**.
79. A. Tonomura, N. Osakabe, T. Matsuda, T. Kawasaki, J. Endo, S. Yano, and H. Yamada, *Phys. Rev. Lett.* 56, 792 **(1986)**.
80. L. P. Levy, G. Dolan, J. Dunsmuir, and H. Bouchiat, *Phys. Rev. Lett.* 64, 2074 **(1990)**.
81. R. Martel, H. R. Shea, and P. Avouris, *J. Phys. Chem. B* 103, 7551 **(1999)**.
82. J. F. Colomer, L. Henrard, E. Flahaut, G. Van Tendeloo, A. A. Lucas, and P. Lambin, *Nano Lett.* 3, 685 **(2003)**.
83. S. Tanda, H. Kawamoto, M. Shiobara, Y. Sakai, S. Yasuzuka, Y. Okajima, and K. Yamaya, *Physica B* 284–288, 1657 **(2000)**.
84. S. Tanda, T. Tsuneta, Y. Okajima, K. Inagaki, K. Yamaya, and N. Hatakenaka, *Nature* 417, 397 **(2002)**.
85. R. A. Römer and M. E. Taikh, *Phys. Stat. Sol.* 221, 535 **(2000)**.
86. W. L. Hughes and Z. L. Wang, *Appl. Phys. Lett.* 86, 043106 **(2005)**.
87. S. Hashimoto and A. Yamaguchi, *J. Am. Ceramic Soc.* 79, 1121 **(1996)**.
88. D. Moore, C. Ronning, C. Ma, and Z. L. Wang, *Chem. Phys. Lett.* 385, 8 **(2004)**.
89. C. Ma, Y. Ding, D. Moore, X. D. Wang, and Z. L. Wang, *J. Am. Chem. Soc.* 126, 708 **(2004)**; *Nature* 427, 497 **(2004)**.
90. F. Vigue, P. Vennegues, S. Vezian, M. Laugt, and J.-P. Faurie, *Appl. Phys. Lett.* 79, 194 **(2001)**.
91. Z. L. Wang, X. Y. Kong, and J. M. Zuo, *Phys. Rev. Lett.* 91, 185502 **(2003)**.
92. R. E. Cohen, *Nature* 358, 136 **(1992)**.
93. Y. Moritomo, A. Asamitua, H. Kuwahara, and Y. Tokura, *Nature* 380, 141 **(1996)**.
94. P. Lacorre, F. Goutenoire, O. Bohnke, R. Retoux, and Y. Laligant, *Nature* 404, 856 **(2000)**.
95. P. W. Anderson and E. Abrahams, *Nature* 327, 363 **(1987)**.
96. J. M. Tarascon and M. Armand, *Nature* 414, 359 **(2001)**.
97. C. C. Homes, T. Vogt, S. M. Shapiro, S. Wakimoto, and A. P. Ramirez, *Science* 293, 673 **(2001)**.
98. X. Wang, J. Zhuang, Q. Peng, and Y. Li, *Nature* 437, 121 **(2005)**.
99. S. O. Brien, L. Brus, and C. B. Murray, *J. Am. Chem. Soc.* 123, 12085 **(2001)**.
100. J. J. Urban, W. S. Yun, Q. Gu, and H. Park, *J. Am. Chem. Soc.* 124, 1186 **(2002)**.
101. Y. Mao, S. Banerjee, and S. S. Wong, *J. Am. Chem. Soc.* 125, 15718 **(2003)**.
102. J. J. Urban, L. Ouyang, M. Jo, D. S. Wang, and H. Park, *Nano Lett.* 4, 47 **(2004)**.
103. G. Xu, Z. Ren, P. Du, W. Weng, G. Shen, and G. Han, *Adv. Mater.* 17, 907 **(2005)**.
104. M. Niederberger, N. Pinna, J. Polleux, and M. Antonietti, *Angew. Chem. Int. Ed.* 43, 2270 **(2004)**.
105. Q. Song and Z. Zhang, *J. Am. Chem. Soc.* 126, 6164 **(2004)**.
106. S. Sun, H. Zeng, D. B. Robinson, S. Raoux, P. M. Rice, S. X. Wang, and G. Li, *J. Am. Chem. Soc.* 126, 273 **(2004)**.
107. T. Hyeon, Y. Chung, J. Park, S. S. Lee, Y. W. Kim, and B. H. Park, *J. Phys. Chem. B* 106, 6831 **(2002)**.
108. Z. L. Wang and Z. C. Kang, Functional and Smart Materials, Plenum Press, New York **(1998)**, Chap. 3.
109. ~~The experimental procedures are protected by an US provisional patent.~~
110. J. A. Dean, Lange's Handbook of Chemistry, 15th edn., McGraw-Hill, Inc., New York **(1999)**.
111. E. W. Wong, P. E. Sheehan, and C. M. Lieber, *Science* 277, 1971 **(1997)**.
112. P. Poncharal, Z. L. Wang, D. Ugarte, and W. A. de Heer, *Science* 283, 1513 **(1999)**.

RESEARCH ARTICLE

113. Z. L. Wang, P. Poncharal, and W. A. de Heer, *Pure Appl. Chem.* 72, 209 **(2000)**.
114. R. P. Gao, Z. L. Wang, Z. G. Bai, W. A. de Heer, L. M. Dai, and M. Gao, *Phys. Rev. Lett.* 85, 622 **(2000)**.
115. Z. L. Wang, Z. R. Dai, R. P. Gao, Z. G. Bai, and J. L. Gole, *Appl. Phys. Lett.* 77, 3349 **(2000)**.
116. L. Meirovich, Elements of Vibration Analysis, 2nd edn., McGraw-Hill, New York **(1986)**.
117. X. D. Bai, E. G. Wang, P. X. Gao, and Z. L. Wang, *Appl. Phys. Lett.* 82, 4806 **(2003)**.
118. W. J. Mai and Z. L. Wang, *Appl. Phys. Lett.* 89, 073112 **(2006)**.
119. E. W. Wong, P. E. Sheehan, and C. M. Lieber, *Science* 277, 1971 **(1997)**.
120. J. P. Salvetat, G. A. D. Briggs, J. M. Bonard, R. R. Bacsa, A. J. Kulik, T. Stockli, N. A. Burnham, and L. Forro, *Phys. Rev. Lett.* 82, 944 **(1999)**.
121. W. J. Mai and Z. L. Wang, *Appl. Phys. Lett.* 89, 073112 **(2006)**.
122. H. Qi, C. Y. Wang, and J. Liu, *Adv. Mater.* 15, 411 **(2003)**.
123. J. Zhou, N. S. Xu, S. Z. Deng, J. Chen, J. C. She, and Z. L. Wang, *Adv. Mater.* 15, 1835 **(2003)**.
124. J. Zhou, N. S. Xu, S. Z. Deng, J. Chen, J. C. She, and Z. L. Wang, *Adv. Mater.* 15, 1835 **(2003)**.
125. R. H. Fowler and L. W. Nordheim, *Proc. R. Soc. London Ser. A* 119, 173 **(1928)**.
126. Y. K. Tseng, C. J. Huang, H. M. Cheng, I. N. Lin, K. S. Liu, and I. C. Chen, *Adv. Funct. Mater.* 13, 811 **(2003)**.
127. R. P. Gao, Z. W. Pan, and Z. L. Wang, *Appl. Phys. Lett.* 78, 1757 **(2001)**.
128. X. D. Bai, E. G. Wang, P. X. Gao, and Z. L. Wang, *Nano Lett.* 3, 1147 **(2003)**.
129. P. Kim, L. Shi, A. Majumdar, and P. L. McEuen, *Phys. Rev. Lett.* 87, 215502 **(2001)**.
130. K. Schwab, E. A. Henriksen, J. M. Worlock, and M. L. Roukes, *Nature* 404, 974 **(2000)**.
131. L. Shi, Q. Hao, C. Yu, D. Kim, N. Mingo, X. Y. Kong, and Z. L. Wang, *Appl. Phys. Lett.* 84, 2638 **(2003)**.
132. S. G. Volz and G. Chen, *Appl. Phys. Lett.* 75, 2056 **(1999)**.
133. P. G. Sverdrup, Y. S. Ju, and K. E. Goodson, *J. Heat Transfer* 123, 130 **(2001)**.
134. E. Comini, G. Faglia, G. Sberveglieri, Z. W. Pan, and Z. L. Wang, *Appl. Phys. Lett.* 81, 1869 **(2002)**.
135. C. Yu, Q. Hao, S. Saha, L. Shi, X. Y. Kong, and Z. L. Wang, *Appl. Phys. Lett.* 86, 063101 **(2005)**.
136. X. D. Wang, Y. Ding, C. J. Summers, and Z. L. Wang, *J. Phys. Chem. B* 108, 8773 **(2004)**.
137. X. F. Duan, Y. Huang, Y. Cui, J. F. Wang, and C. M. Lieber, *Nature* 409, 66 **(2001)**.
138. Z. H. Zhong, F. Qian, D. L. Wang, and C. M. Lieber, *Nano Lett.* 3, 343 **(2003)**.
139. R. S. Yang, Y. L. Chueh, J. R. Morber, R. Snyder, L. J. Chou, and Z. L. Wang, *Nano Lett.* 7, 269 **(2007)**.
140. M. H. Zhao, Z. L. Wang, and S. X. Mao, *Nano Lett.* 4, 587 **(2004)**.
141. Z. L. Wang and J. H. Song, *Science* 312, 242 **(2006)**.
142. X. D. Wang, J. H. Song, J. Liu, and Z. L. Wang, *Science* 316, 102 **(2007)**.
143. J. Zhou, N. S. Xu, and Z. L. Wang, *Adv. Mater.* 18, 2432 **(2006)**.

Received: xx Xxxx xxxx. Revised/Accepted: xx Xxxx xxxx.